UNIVERSITY OF OKLAHOMA

GRADUATE COLLEGE

DESIGN AND VALIDATION OF MEASUREMENT PROCEDURES FOR

TIME-VARYING SCATTERERS AND ANTENNAS

A THESIS

SUBMITTED TO THE GRADUATE FACULTY

in partial fulfillment of the requirements for the

Degree of

MASTER OF SCIENCE

By

KYLE KANALY
Norman, Oklahoma
2022

DESIGN AND VALIDATION OF MEASUREMENT PROCEDURES FOR
TIME-VARYING SCATTERERS AND ANTENNAS

A THESIS APPROVED FOR THE
SCHOOL OF ELECTRICAL AND COMPUTER ENGINEERING

BY THE COMMITTEE CONSISTING OF

Dr. Jessica Ruyle, Chair

Dr. KC Kerby-Patel

Dr. Jay McDaniel

Acknowledgments

I want to begin by thanking my co-advisors Dr. Jessica Ruyle and Dr. KC
Kerby-Patel, for their guidance and patience during my journey to complete my
master's degree. Because of their mentorship, I have grown to feel empowered to
pursue my goals and aspirations as both an engineer and a person.

In my time at the ARRC I have had the opportunity to meet some of the most
wonderful people. I want to thank Stephen Bass for his mentorship, friendship, and
willingness to answer the many questions I bugged him with every other hour.
Stephen, I know that you will be a great professor, and I hope you have a great time
getting there. I also want to thank Clayton Blosser for his friendship, humor, and his
willingness to help anyone with anything at any time. Clayton, I also want to
congratulate you and Celeste on your recent marriage. I wish you two a lifetime of
happiness. To the rest of the Ruyle Group, I want to thank you for all the memories
and the help you provided in getting me to where I am today. I also want to thank
Rylee G. Mattingly for his friendship and constant pool of random knowledge. You
have served as an excellent example of someone with an incredible personal drive and
a sense of responsibility, and I am glad to call you my friend. I want to thank Rachel
Jarvis for her friendship and advice over the past several years. I know you will be
great at whatever you do. To everyone else at the ARRC, thank you for the memories
and lessons you have provided.

To my parents, Jack and LuAnn Kanaly, who have supported me my whole life and

enabled and encouraged me to pursue the person I want to be in life. I love you both, and I can never repay or thank you enough for the life you have given me. To my life partner Julia Nguyen, I would not be the man and partner I am today without you and your patience, kindness, and love. You are my best friend, and I am excited to start this next phase of our lives. I love you with my whole heart, and I can't wait to see our lives together. Finally, to my late dog Molly, you were my silly Molly dog, and you got me through so much in my life. I miss you, and I'll remember you forever.

Table of Contents

viii

List of Tables

List of Figures

Abstract

There is an interest in establishing performance metrics for time-varying antennas. However, quantifying the realized performance of a time-varying antenna requires considerations not necessary in LTI measurements as many metrics and electromagnetic properties, often utilized in traditional LTI antenna measurements, are not applicable to a non-LTI antenna measurement. It is expected from earlier work that antennas loaded with time-varying components will radiate power at many frequencies other than the excitation frequency when excited by a pure-toned signal. Two conventionally used metrics to calibrate antenna performance are monostatic backscatter and effective aperture. Using only traditional measurement methodologies and definitions are not ideal as they are only concerned with a device's performance at the incident frequency. However, the existing quantities and their measurement methodology can be redefined to account for the time-varying antenna's non-LTI behavior. This work presents a methodology for performing cross-frequency backscatter and effective aperture measurements of an antenna loaded with a time-varying component. These techniques are demonstrated by measuring two switch-loaded bowtie antennas operating at four different switching frequencies. These techniques are also validated and supported by comparing the measurements to the simulation results provided by the electromagnetic solvers XFdtd and CM-MoM.

Chapter 1

Introduction

A device assumed to be linear and time-invariant (LTI) must be structurally and materially constant across time. If these criteria are met, and a device is LTI, its performance will be more easily predicted. Due to this increase in predictability, the LTI assumption is standard in conventional antenna design, such that many of the commonly accepted limitations on antenna performance were even derived adhering to the LTI assumption [1], [2], [3], [4]. It is possible that a non-LTI antenna, specifically a time-varying one, will not be governed by the same performance limitations as an LTI device because the referenced limitations themselves carry an LTI assumption. However, to verify that a time-varying device can or has exceeded the performance of an LTI device requires special considerations as most conventional antenna theory, parameters, and measurement methodologies are also rooted in an LTI assumption.

In addition to potentially exceeding limitations in performance, time-varying antennas are expected to exhibit unique radiation characteristics due to their non-LTI nature. Over the decades, researchers in [5] [6] [7] [8] have used both frequency and time-domain modeling approaches to analytically study the response of time-varying scatterers. These models yield an expectation that when excited at a single frequency, a time-varying scatterer will exhibit a response at the excitation frequency in addition to multiple other frequencies. These additional frequency responses are harmonics of the

excitation frequency and are determined by the structure's time-varying rate, or "pumping frequency" [7]. An example of a time-varying antenna's expected multiple frequency scattering response is shown in Figure 1.1. The frequencies that a time-varying scatterer is expected to respond at, f, when excited at one frequency is determined by the relationship between that excitation frequency, f_0, and the device's time-varying rate, f_p,

$$f = f_0 + nf_p .$$
(1.1)

Fig. 8.   Electric far field scattered from a dipole antenna illuminated by a 16-MHz sinusoidal wave and loaded by a resistance varying in a sinusoidal fashion at 4 MHz.

Fig. 9.   Spectrum of the waveform of Fig. 8.
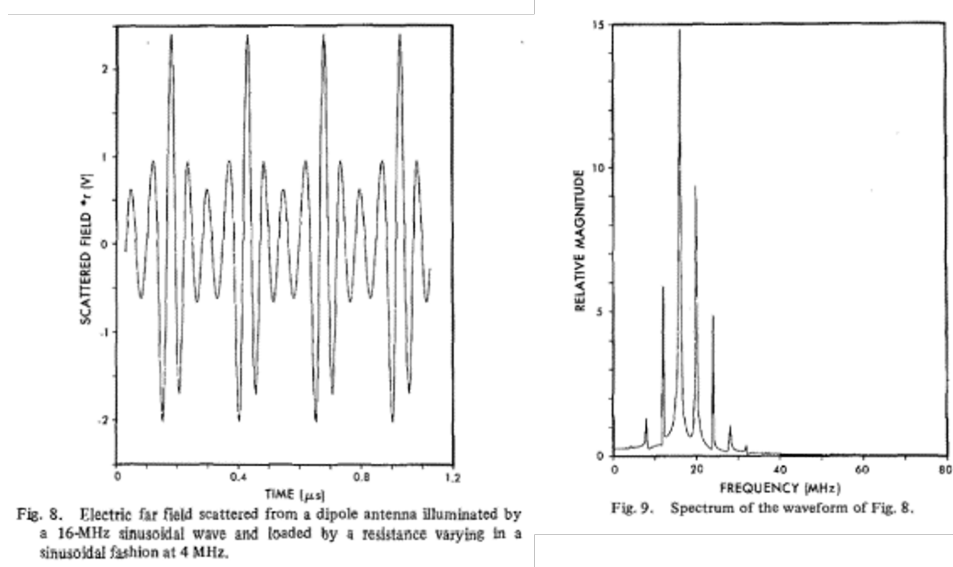
Figure 1.1: Spectrum of a modulated waveform presented in [7]

When it comes to time-varying antennas, researchers have seldom provided measurements of such a kind of device. One example is in [9], wherein the current through an antenna's time-varying load was measured and compared to the expected as a means to highlight the accuracy of the author's novel diode model. Another example is in [10], where the author provides measurements of the voltage across a switching capac-

2

itor along with an uncalibrated received power measurement to highlight the achieved functionality of their novel electrically coupled loop antenna, ECLA, design. To this date, the measurements provided in [9] and [10] are the antenna community's furthest extent at quantifying a time-varying antenna's realized performance, and despite serving their intended purpose, the presented results fail to provide a method of a calibrating a time-varying antenna measurements.

Several issues are currently facing the time-varying community after considering the community's prior work. One of the major issues is the lack of any parameters that one can use to calibrate their time-varying antenna measurements. This problem is addressed in the final chapter of [10], wherein the author lists a desire for someone to adapt conventional frequency parameters for time-varying antennas in future work as a significant priority. In addition to the lack of calibration parameters, the time-varying community lacks any established measurement techniques and methodologies, and given their expectedly unique performance, time-varying antennas will likely require unique nuance during measurements. Without these needs addressed, the time-varying community will likely be hindered in their pursuit of novel breakthroughs with time-varying antennas. Thus, researchers are needed who will tackle these issues and provide the tools for future researchers.

1.1 Project Goal

This thesis aims to support the growing interest in time-varying scatterers and radiators by providing modified forms of two conventionally used antenna parameters. The updated forms are labeled "cross-frequency" in reference to the relationship it forms with a device's performance across a series of frequencies and an assumed pure-toned excitation. The first half of this thesis focuses on cross-frequency backscatter, which

is a modified form of monostatic backscatter free of an LTI assumption. A measurement methodology unique to cross-frequency backscatter is developed and used to gain measurements of a time-varying bowtie antenna. Those measurements are compared to simulation results to validate the accuracy of the measurement methodology. The second half of the thesis introduces a cross-frequency effective aperture term, a modified form of the well-known term effective aperture. A measurement methodology designed for cross-frequency effective aperture is developed and used to obtain measurements of the time-varying bowtie antenna loaded with a feeding network. These measurements are also compared to their expected performance, which is obtained via simulation, to validate the methodology's accuracy.

The second chapter will introduce the term monostatic backscatter, which is used as the backbone for the development of cross-frequency backscatter. The chapter also covers several lessons on how to obtain accurate scattering measurements. The third chapter introduces cross-frequency backscatter and a detailed discussion over the measurement methodology. The fourth chapter covers applying the cross-frequency backscatter methodology along with comparisons to simulation results. The fifth chapter introduces cross-frequency effective aperture and the term's measurement methodology. The measurement process is then applied, and the resulting measurements are compared to simulation results.

Chapter 2

Monostatic Backscatter and Methodology

This chapter will lay the groundwork for the eventual research into cross-frequency parameters by first introducing the concept of monostatic backscatter and the measurement methodology utilized to obtain measurements with an accuracy of 0.5 dBsm. The essential role that the multipath compensation techniques of background subtraction and time gating played in obtaining the desired level of accuracy in backscatter measurements is also highlighted.

2.1   Introduction to Monostatic Backscatter

Backscatter is used to quantify a target's efficiency at scattering power in a given direction given a power density incident to the target's surface at a known angle of incidence [11]. There exist several forms of backscatter used in the field of radar. One of the more common forms, monostatic backscatter, relates to backscatter measured using a monostatic radar system. A monostatic radar system uses either a single antenna for both transmitting and receiving or uses two collocated antennas, as reflected in Figure 2.1. Notably, if the two antenna approach is used, one must not violate the collocation assumption by having too much space between the antennas, which classifies the system as bistatic.
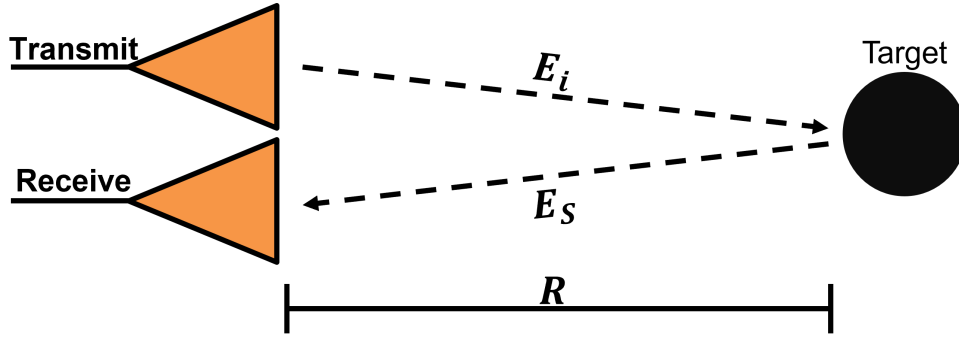
Figure 2.1: The two most common forms of radar systems, monostatic and bistatic.

Out of every form of backscatter, monostatic backscatter serves as the preferred form of the quantity to use in experimental measurements [11]. This notion was the reason for using the monostatic term as the basis for the scattering measurements. The process of evaluating a device's realized monostatic backscatter is done using the radar range equation, as the formal expression for backscatter, Eq. (2.1), does not efficiently apply to an actual measurement. In Eq. (2.1), the distance between the target and radar is R, the scattered field is E_s, and the incident field is E_i.

$$\sigma(f) = \lim_{R \to \infty} 4\pi R^2 \frac{|E_s(f)|^2}{|E_i(f)|^2} \ . \tag{2.1}$$

2.1.1 General Backscatter Expression

The general backscatter expression used for measurements is formed by rearranging the radar range equation to isolate for the backscatter quantity (σ). Backscatter is equal to the received power (P_r), range, and system loss (L) normalized by the transmit power (P_t), transmit and receive antenna gain (G_t) (G_r), and the operation wavelength (λ).

$$\sigma = \frac{P_r R^4 (4\pi)^3 L}{P_t G_t G_r \lambda_r^2} \ . \tag{2.2}$$

The dependent terms on the right side of Eq. (2.2) are grouped to make the general expression better suited for measurement application. These grouped terms are known as the calibration factor (K). As the name implies, the calibration factor is used to calibrate the power received to power transmitted ratio in a backscatter measurement. The calibration factor does operate on two fundamental limitations. First, the factor is only applicable if the radar system is physically unchanged between acquisition and use. Second, the factor's accuracy is inversely related to the time between acquisition and the uncalibrated measurement. While this relationship is minimal, it can lead to a source of error in measurements if enough time passes.

$$\sigma = \frac{P_r}{P_t} K \ .$$
(2.3)

2.2 Radar Setup

The monostatic radar used in this thesis was designed with both monostatic and cross-frequency backscatter measurements in mind. A diagram of the system is shown Figure 2.2. The system utilizes two collocated antennas, one for transmitting and another for receiving. Both of the antennas were NARDA S-Band standard gain waveguide horn antennas and were fed using 65 foot long 50 ohm coax cables. The same antenna model and feeding cables are used on transmit and receive as this allowed for physical symmetry assumptions during later work that would not be valid otherwise. All signals were transmitted, received, and processed using the Keysight N9928A model Field Fox. The choice to use a field fox and this specific model was because the device offered both spectrum and network analyzer capabilities, which was vital for cross-frequency measurements. Finally, a 20 dB amplifier was included on the transmit chain to increase the power of the transmit signal to insure a sufficient signal-to-noise ration

7

(SNR) on receive. During early cross-frequency measurements the signal's SNR was too low, which hindered the field fox's ability to measure the harmonics.
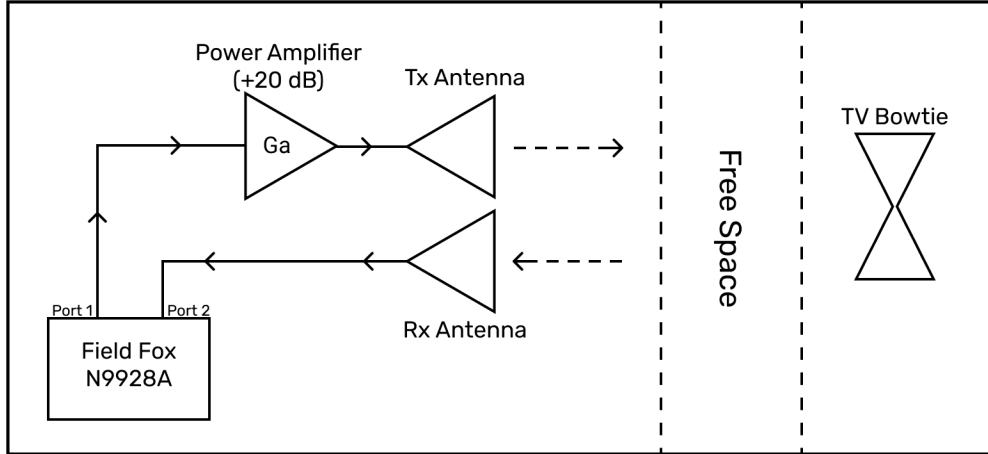
Figure 2.2: The monostatic radar used for the monostatic and cross-frequency backscatter measurements

2.3 Measurement Process

The process of taking a monostatic measurement is outlined in Figure 2.3 and begins with the Field Fox introducing a pure-toned plane wave into the radar setup shown in Figure 2.2. This plane wave will then travel to the target or device under test (DUT) and illuminate the surface, resulting in power scattering and traveling back to the radar. The power scattered off the target is measured by the receive chain and is then normalized against the power transmitted, forming an S_{21} measurement. The S_{21} measurements, which are kept in their real and imaginary forms, are processed using the multipath compensation techniques background subtraction and time gating [12]. These compensation techniques isolate the DUT's response from undesirable responses. The isolated S_{21} measurement is then calibrated to backscatter using Eq. (2.3), where the S_{21} measurement is normalized against the system's calibration factor, K. The process of

extracting the calibration factor is discussed further in the next section, along with a procedure to evaluate quantity's accuracy.
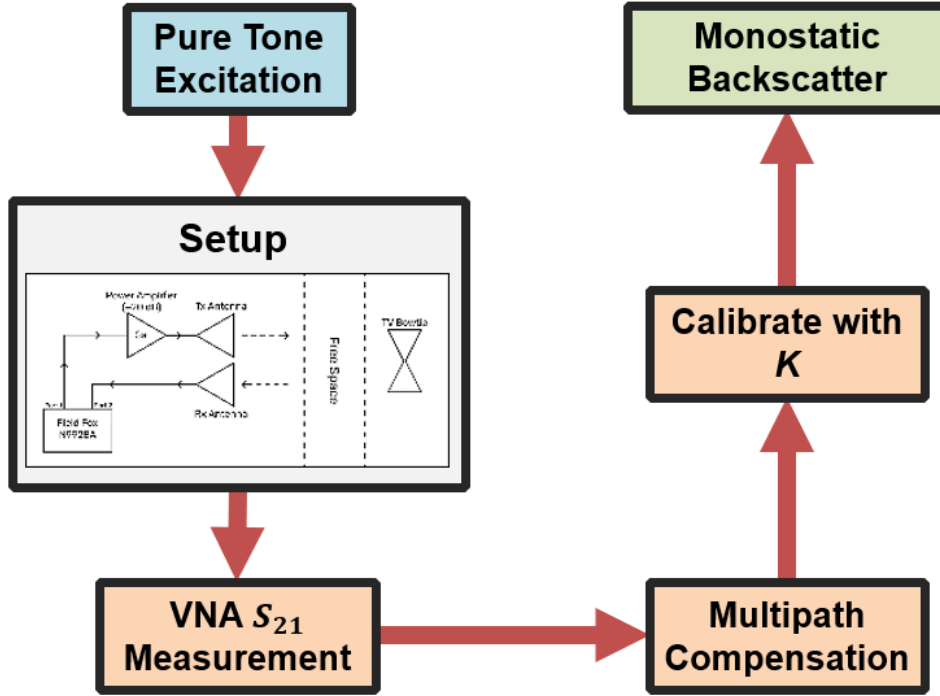
Figure 2.3: The flow of a monostatic measurement

2.3.1 The Calibration Factor

A radar system's calibration factor is expressed in Eq. (2.4) as a target's expected backscatter normalized by an S_{21} measurement

$$K = \frac{\sigma}{S_{21}} \ .$$
<div align="right">(2.4)</div>

Utilizing Eq. (2.4) to find a system's calibration factor is possible through the use of calibration objects, which are objects with backscatter values known through calculations [13]. The Mie series was used to calculate the calibration objects expected

backscatter [14],

$$\sigma = \frac{\lambda^2}{\pi} \left| \sum_{n=1}^{\infty} (-1)^n (n + \frac{1}{2})(b_n - a_n) \right| . \qquad (2.5)$$

where

$$a_n = \frac{j_n(ka)}{h_n(ka)}$$

$$b_n = \frac{kaj_{n-1}(ka) - nj_n(ka)}{kah_{n-1}(ka) - nh_n(ka)}$$

$$h_n = j_n + iy_n$$

In Eq. (2.5) k is the wavenumber ($k = \frac{2\pi}{\lambda}$), a is the sphere's radius, and j_n and y_n are n-order Bessel functions [15].

The calibration object used to obtain the calibration factors in this thesis was a 12-inch sphere. A second calibration sphere with a diameter of 6 inches was used to assess the accuracy of the calibration factors. The accuracy of the calibration factors was quantified using the average difference between the second sphere's measured backscatter and its calculated backscatter,

$$\Delta\sigma = \frac{\Sigma[\sigma_{meas} - \sigma_{expt}]}{n} . \qquad (2.6)$$

In Eq. (2.6) the measured and calculated backscatter are represented as σ_{meas} and σ_{expt} respectively and the number of data points is n. The tolerated amount of mean difference between the measured and expected depends on the intended application of

the radar system. The measurement shown in Figure 2.4 exhibits an average difference of 0.4253 dBsm to the calculated, which satisfied my benchmark of 0.5 dBsm.

Measured vs Expected
Backscatter of a 12-Inch Metalic Sphere
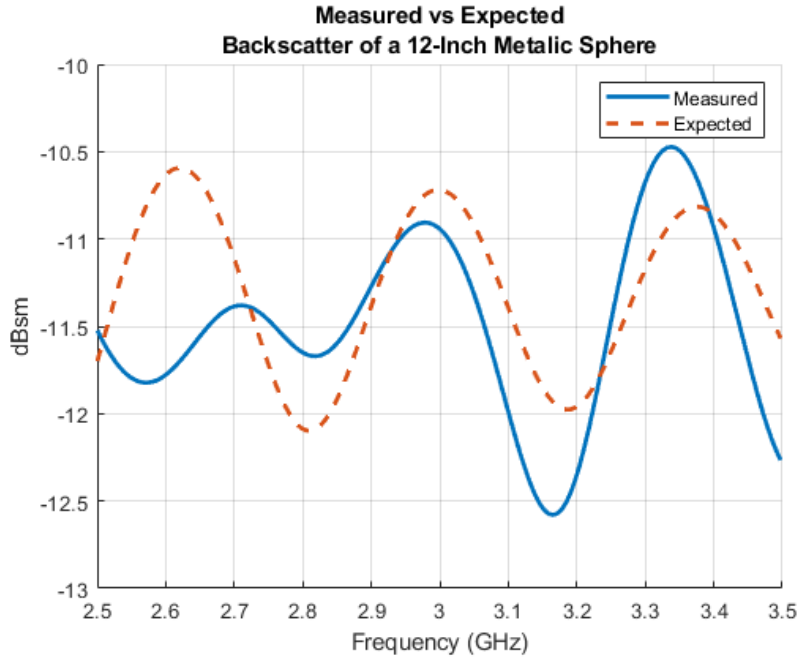
Figure 2.4: Comparing the measured backscatter of a 12-inch sphere to the expected.

2.3.2   Antenna Coupling and Multipath Compensation

In any backscatter measurement, there will be undesired signals known as multipath signals that will interfere with the accuracy of the measurement. Multipath signals, sometimes known as clutter, are any signals other than the DUT's scattering response. For the monostatic radar, as Figure 2.5 shows, the most influential source of clutter is the coupling between the transmit and receive antennas, reflections from the target's mounting structure, and reflections from the back wall.
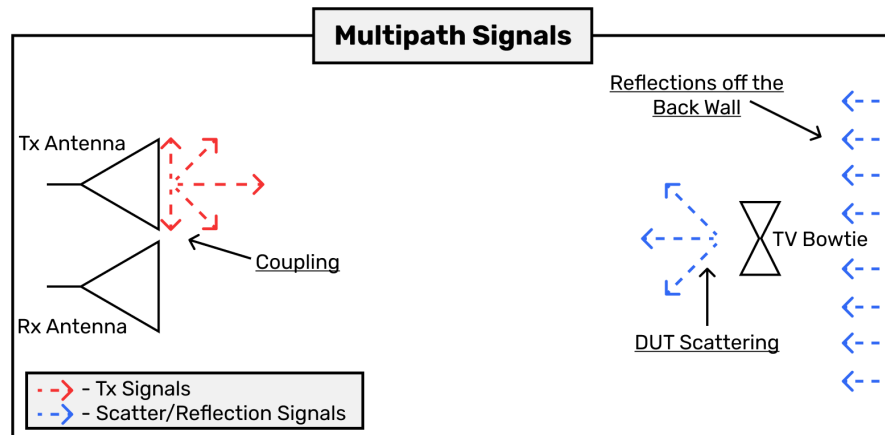
Figure 2.5: The generalized process of obtaining LTI K

The impact of these multipath signals on measurement accuracy is demonstrated in Figure REF, where the pattern of a processed and unprocessed backscatter measurement is compared to the the target's expected backscatter. The pattern of both plots should show some level of agreement, but due to multipath and coupling signals overshadowing the target's response there is none. However, through the use of background subtraction and time gating, the target's response can be isolated from the cluttered S_{21} measurement. This isolated response results in a backscatter measurement whose pattern shows improved agreement with the expected.
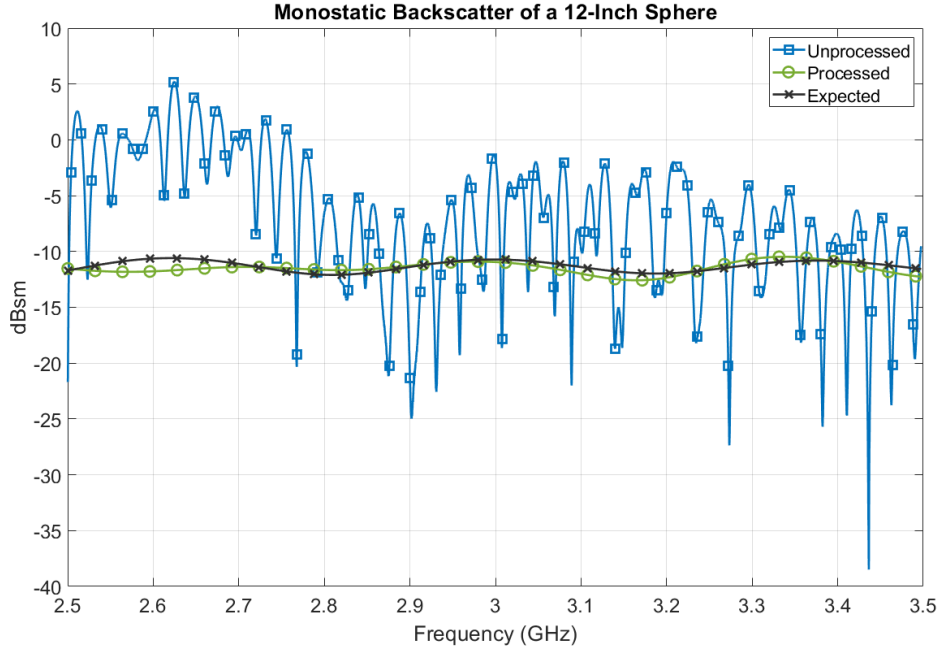
Figure 2.6: The beneficial impact of multipath compensation, demonstrated by comparison the patterns of a raw S_{21} measurement, the isolated form of the same S_{21} measurement, and the expected backscatter for the given target.

Background Subtraction

Background subtraction is a signal processing technique wherein an "empty chamber" measurement is subtracted from the actual DUT measurement [12]. As the name implies, the empty chamber measurement is a reference measurement taken with only the DUT not present. If the empty chamber measurement is taken correctly, the main difference between the DUT and the empty chamber measurements should be the actual response from the target, as Figure shows. Before subtraction, both measurements need to be converted to their in-phase and quadrature ($I + jQ$) forms.

13
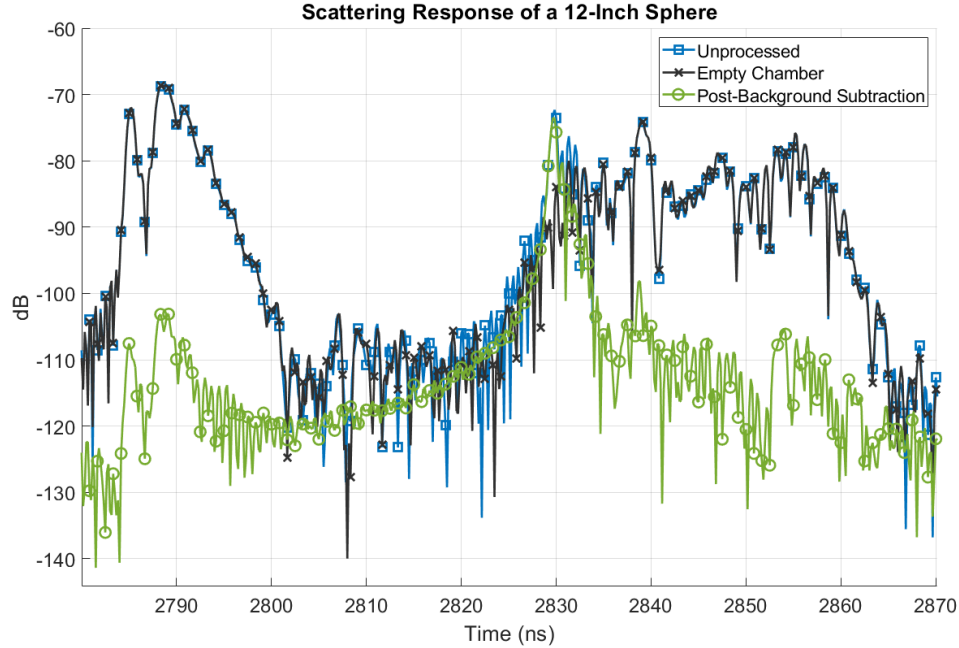
Figure 2.7: The result of applying background subtraction on a cluttered S_{21} measurement.

As Figure 2.7 shows, background subtraction will not entirely eliminate multipath signals from the DUT measurement, but it does heavily reduce their presence. This reduction makes it easier to spot the target's response. In some cases, like in Figure 2.7, background subtraction will reveal portions of the target's response previously not visible as they were overshadowed by clutter.

Time-Gating

Time-gating is a signal processing technique that isolates a target's response from a cluttered measurement via a windowing function. The windowing structure and temporal location are determined after visual inspection of the post-background subtraction S_{21} measurement. There are several options for the window's structure. However, a classic

boxcar function centered around the target's response is sufficient for the desired measurement accuracy.
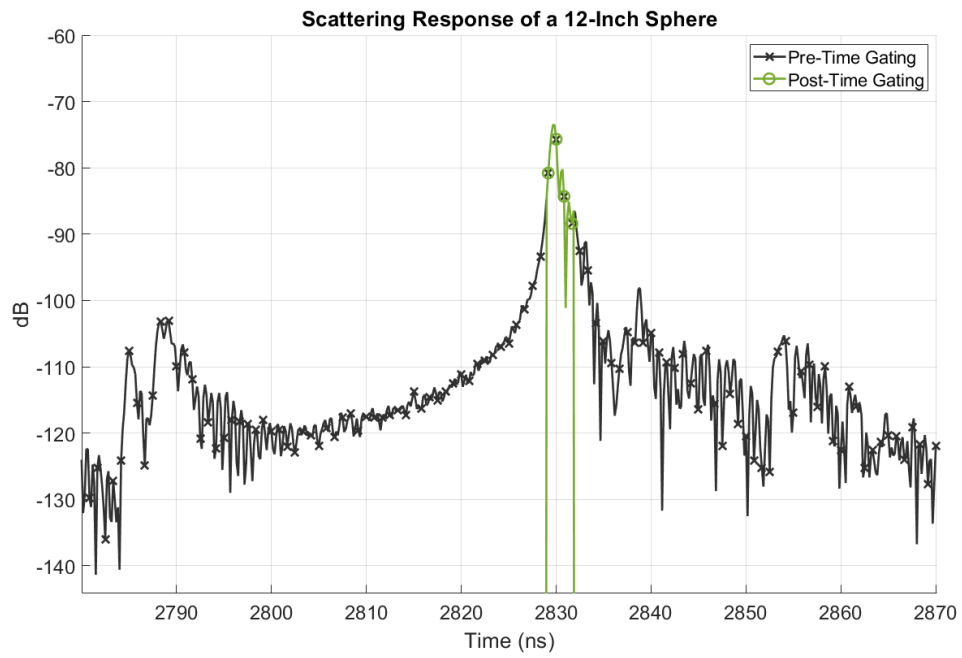
Figure 2.8: Visualization of applying a time-gate onto an S_{21} measurement post background subtraction.

Chapter 3

Cross-Frequency Backscatter and Methodology

The previous chapter, introduced the concept of monostatic backscatter along with a breakdown and demonstration of one applicable measurement methodology for backscatter measurements. The capabilities of a realized monostatic radar system is shown to produce measurements to the desired accuracy of 0.5 dBsm when coupled with background subtraction and time-gating. This chapter introduces the concept of cross-frequency backscatter, a modified form of monostatic backscatter designed to be more appropriate for the expected performance of a time-varying scatterer. Discussion is provided on the need for a cross-frequency term along with the derivation of the new cross-frequency term. Finally, a cross-frequency normalizing term is acquired, and discussion is provided on how to utilize the term to convert the LTI form of the calibration factor into the needed cross-frequency form.

3.1 Introduction to Cross-Frequency Backscatter

It was established in the previous chapter that backscatter is a term that describes a ratio of the field density scattering off of an object to the incident field density, normalized by a far-field distance. Because the conventional definition operates under an LTI assumption the term is limited to quantifying only the field densities scattering at

the incident frequency. This restriction is an issue when working with time-varying scatters as they are expected to scatter across frequencies at harmonic intervals of the incident frequency. Thus, to normalize this behavior of interest, a novel redefinition of monostatic backscatter is needed.
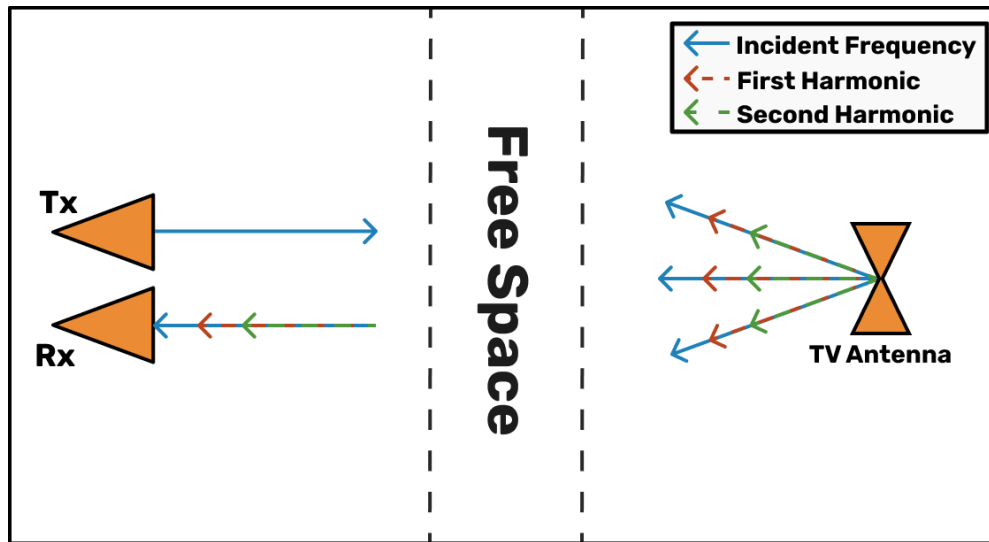
Figure 3.1: The expected scattering performance of a TV antenna. A situation were power is expected to be received a the incident frequency and harmonics

The term's frequencies of interest were redefined considering that the issue with the conventional form of backscatter is the term's inability to calibrate multiple frequency measurements using power transmitted at one frequency. The cross-frequency form of backscatter has been defined such that it quantifies a relationship between the scattering field densities across a vector of receiving frequencies and the pure-toned incident field density. This new form is not limited to one incident frequency. If needed, the new expression can support a vector of transmission frequencies. However, this would transform the receive terms into two-dimensional matrices, sporting a vector of values for every transmission frequency

$$\sigma(f_i, \vec{f_j}) = \frac{P_R(\vec{f_j})}{P_T(f_i)} K(f_i, \vec{f_j}) .$$
(3.1)

In Eq. (3.1) the received power has been changed from Eq. (2.3) to a vector notation ($\vec{P_r}$) to denote the term's inclusion of measurements at multiple frequencies. The backscatter and calibration factor terms have also been updated to vector notation ($\vec{\sigma}$) ($\vec{K}$)as a means to distinguish them from their conventional forms.

3.2   Cross-Frequency Methodology

As Figure 3.2 shows, the process of taking a cross-frequency backscatter measurement begins by introducing a pure-toned waveform via an incident field into the radar system shown in the diagram's Setup panel. This pure-toned waveform will then induce a current along the surface of the time-varying DUT. The induced current will then be modulated according to the pumping frequency, causing the DUT to re-radiate power at the incident and harmonic frequencies. That cross-frequency performance will then be recorded via two measurement methods in order to produce a proper reflection of the DUT's performance. The first measurement is taken with a spectrum analyzer, which records the time-varying response across a vector of frequencies. The second measurement is a network analysis, which produces an accurate report on the incident frequency measurement.
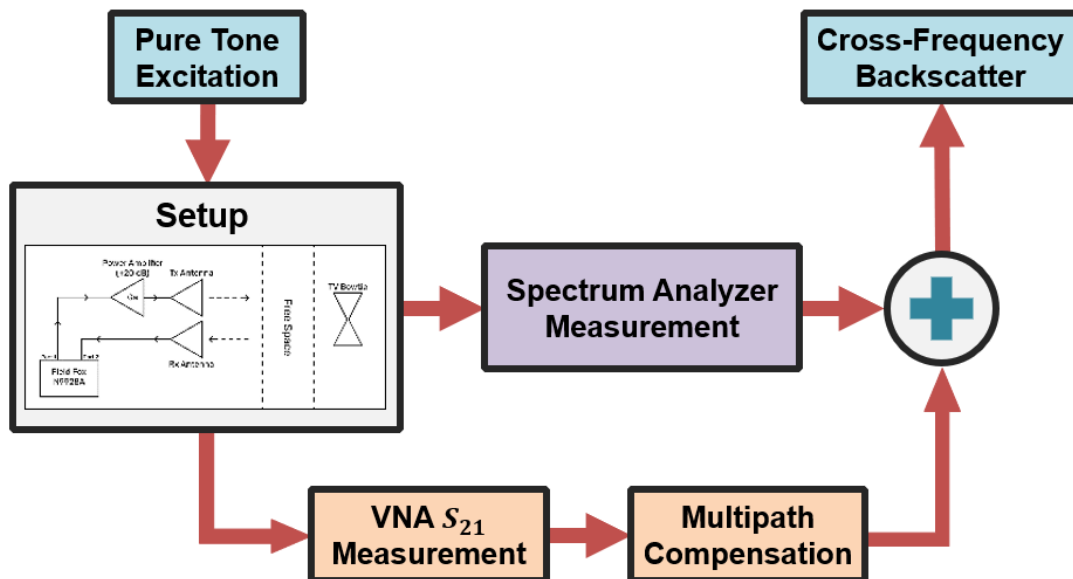
Figure 3.2: Flow chart depicting the general methodology used in cross-frequency backscatter measurements

3.2.1   Why Two Measurements?

The measurement methodology utilizes both spectrum and network analyzer measurements due to the impact of multipath signals. While measurements with the spectrum analyzer capture a time-varying device's response across multiple frequencies, the measurement at the excitation is heavily impacted by multipath signals as seen in Figure 3.3. This impact is an issue as spectrum measurements lack any phase information which prevents multipath compensation. As such, an S_{21} measurement is taken to provide a measurement of the device's response with phase information. The uncalibrated S_{21} measurement is then isolated from the clutter, and the response at the excitation frequency is spliced into the uncalibrated spectrum measurement.
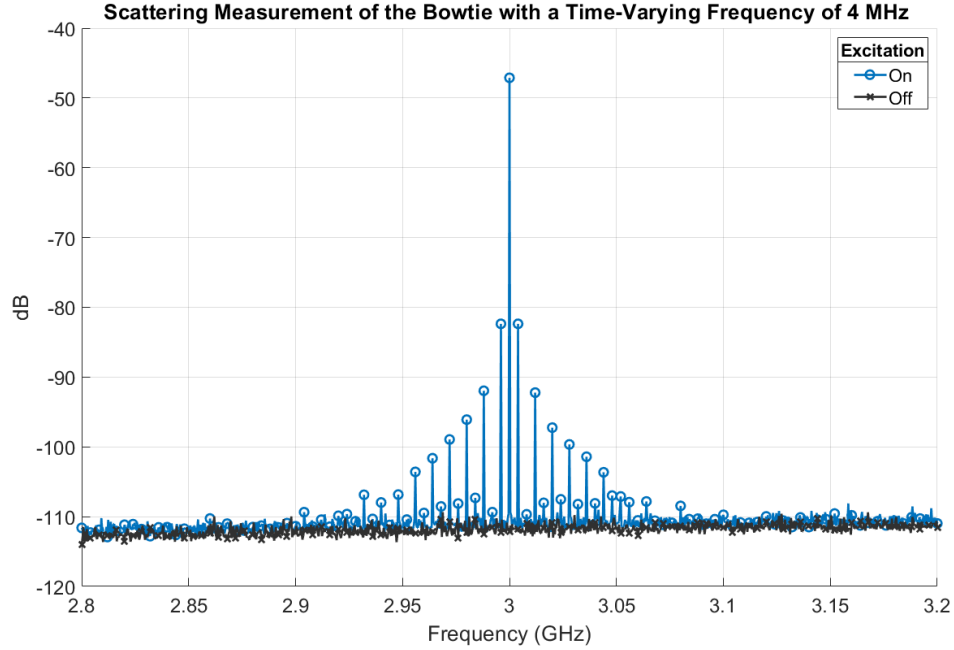
Figure 3.3: An uncalibrated scattered power measurement of a time-varying antenna excited at 3 GHz.

The impact of multipath signals on harmonic measurements comes into question, given the significant impact multipath signals have on the raw incident frequency measurement. There is no concern regarding multipath signals skewing the harmonic measurements since the foam used in the ARRC's anechoic chamber is rated to dampen signals by 30 dB, which means every harmonic will drop below the noise floor after coming into contact with the chamber walls since no harmonic is 30 dB above the chamber noise floor.

3.3 The Cross-Frequency Calibration Factor

A cross-frequency calibration factor was required to extract cross-frequency backscatter. This new form is obtained via the cross-frequency ratio, which is defined as the

difference between the conventional and cross-frequency forms of the calibration factors. The cross-frequency form of the factor is obtained by multiplying the conventional form by the ratio,

$$K(\vec{f_j}, \vec{f_j})X(f_i, \vec{f_j}) = K(f_i, \vec{f_j}) . \tag{3.2}$$

The cross-frequency calibration ratio, X, represents the difference between the pre-existing LTI calibration factor and the desired cross-frequency form. Prior to the derivation of the ratio three key assumptions were established. The first assumption states that the frequency vector corresponding to the LTI calibration factor is the same vector of frequencies used for the receive terms in the cross-frequency measurement, $f = \vec{f_j}$. The second assumption states that the system loss term in Eq. (2.4) is the product of both the receive and transmit chain losses, $L(f_{Tx}, f_{Rx}) = L_T(f_{Tx})L_R(f_{Rx})$. The third assumption states that radar system and range are physically constant between measurements types.

The derivation begins by expanding both calibration factors into their full expressions to identify and cancel any terms constant between both forms,

$$\frac{R^4(4\pi)^3 L(\vec{f_j}, \vec{f_j})}{G_T(\vec{f_j})G_R(\vec{f_j})\vec{\lambda_j}^2}X(f_i, \vec{f_j}) = \frac{R^4(4\pi)^3 L(f_i, \vec{f_j})}{G_T(f_i)G_R(\vec{f_j})\vec{\lambda_j}^2} .$$

The only terms not constant between the two forms are the transmit losses (L) and the transmit antenna's gain (G_t),

$$\frac{L(\vec{f_j}, \vec{f_j})}{G_T(\vec{f_j})}X(f_i, \vec{f_j}) = \frac{L(f_i, \vec{f_j})}{G_T(f_i)} .$$

the ratio term $\vec{X}$ is then isolated,

$$x(f_i, \vec{f}_j) = \frac{L_T(f_i)G_T(\vec{f}_j)}{L_T(\vec{f}_j)G_T(f_i)} \ .$$

(3.3)

Finding the cross-frequency ratio requires knowledge of the transmit antenna's gain (G_t) and the loss in the transmit signal (L_t), both across the receive frequency vector. The transmit antenna's gain is a known quantity, as the antenna is a standardized model designed for S-band operation and has its calcualted performance specified in the device's datasheet. The expected gain for the transmit antenna is shown in Figure 3.4. Notably, the plot shown in Figure 3.4 depicts the idealized performance of the antenna, which is not an accurate reflection of the realized device. However, any inefficiencies in the realized device's performance would be reflected in the transmission loss term.
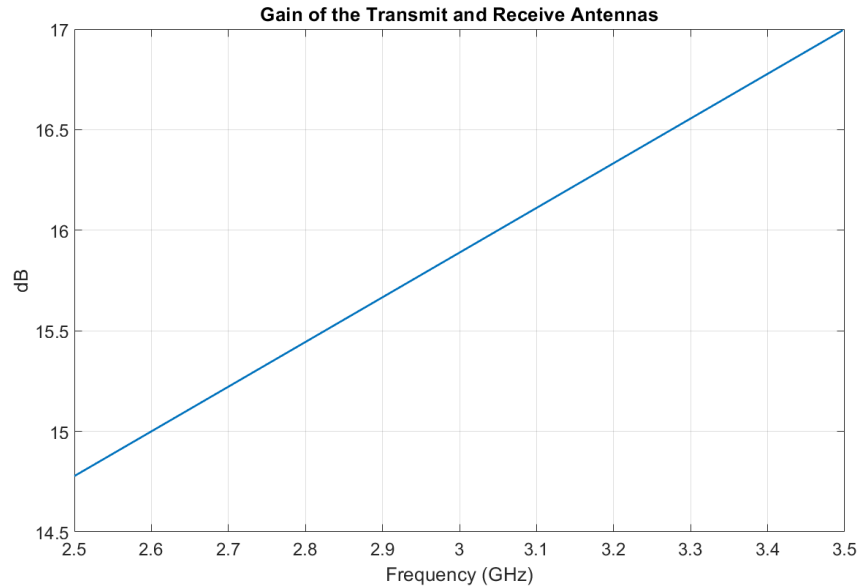
Figure 3.4: The gain of the NARDA developed S-Band Horn Antenna, model 644, used as the transmit antenna in my radar system

Evaluating the amount of loss produced in only the transmit chain is a task that requires further discussion as loss, in any regard, is a sensitive quantity and is influenced

by many parameters, not all of which are controllable by the radar user. Two common contributors that can be easily measured are cable attenuation and connector mismatch. However, these losses are only a percentage of the total loss in a transmit chain, and the summation of both measurements will fail to accurately reflect the system's total loss. A better approach to obtaining the L_t value is to find the superposition of total loss in the transmit propagation.

3.3.1   System Loss Representation and Acquisition

An excellent way to represent the loss in a system, which has been established as the product of the transmit and receive chain losses, is as an MxN matrix, Figure 3.5, whose rows and columns change with the transmit and receive frequencies, respectively. Every element in this matrix represents the total system loss at any given transmit and receive frequency measurement. The main diagonal of the loss matrix, which refers to the elements where $i = j$, represents the loss of the radar system during an LTI operation. A single row from the matrix, where i is a constant value and j is a vector of length n, represents the radar system's loss during a cross-frequency operation.
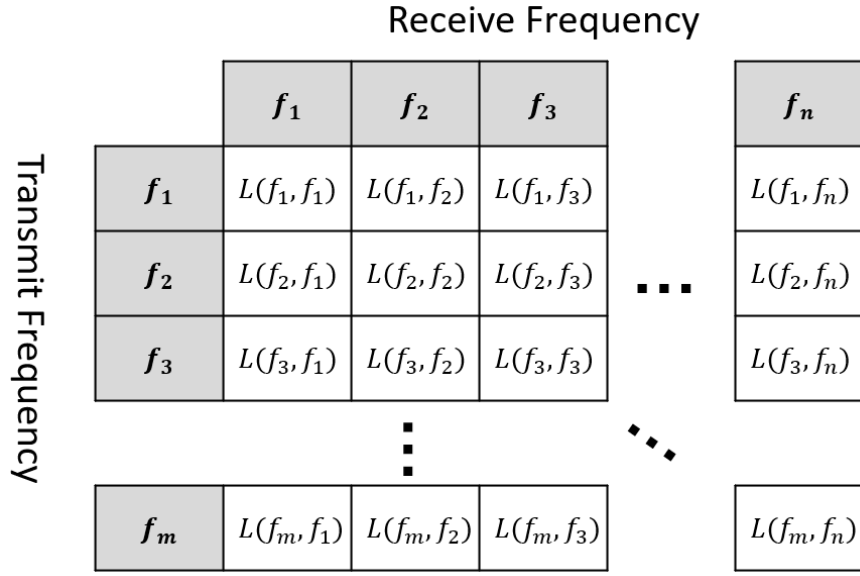
Figure 3.5: System loss represented as a 2-D matrix

An LTI system's loss can be acquired by first finding a system's calibration factor and then isolate the system's losses (L_s),

$$L_S(f) = \frac{K(f)G_T(f)G_R(f)\lambda^2}{R^4(4\pi)^3} \ . \tag{3.4}$$

This approach to finding a system's loss does require prior knowledge of the other system parameters. However, most of these values are either provided via datasheets or can be found via simple physical measurements.

Once the system loss is obtained, a common assumption is that the transit and receive chain losses can be treated equal due to physical symmetry. However, this assumption is not applicable for my radar system as the transmit chain is equipped with an amplifier, Figure **??**. The utilization of an amplifier on only the transmit side breaks physical symmetry and bars the $L_T = L_R$ assumption. Thus, to isolate the transmit chain losses, the term needed to find the calibration factor ratio, requires knowledge of

the loss in the system's receive chain,

$$L_T(\vec{f_j}) = \frac{K(\vec{f_J})G_T G_R \vec{\lambda_j}^2}{(4\pi)^3 R^4 L_R(\vec{f_J})} .$$ (3.5)

To obtain the amount of loss in the system's receive chain, the amplifier is removed from the radar's transmit chain, as reflected in Figure 3.6. Due to both the transmit and receive chains using the same model and length of cabling, physical symmetry was produced in the system by removing the amplifier from the transmit side. The use of the $L_T = L_R$ assumption was enabled by establishing the physical symmetry,

$$L_R(\vec{f_j}) = L_T(\vec{f_j}) = \sqrt{\frac{K(\vec{f_J})G_T G_R \vec{\lambda_j}^2}{(4\pi)^3 R^4}} .$$ (3.6)

The only difference between the symmetric and the asymmetric setups was the presence of the amplifier on the transmit side since the same model and length of coax cabling was used in the transmit and receive chains. The amount of loss measured in the physically symmetrical system's receive chain is equal to the physically asymmetric system's receive chain loss.
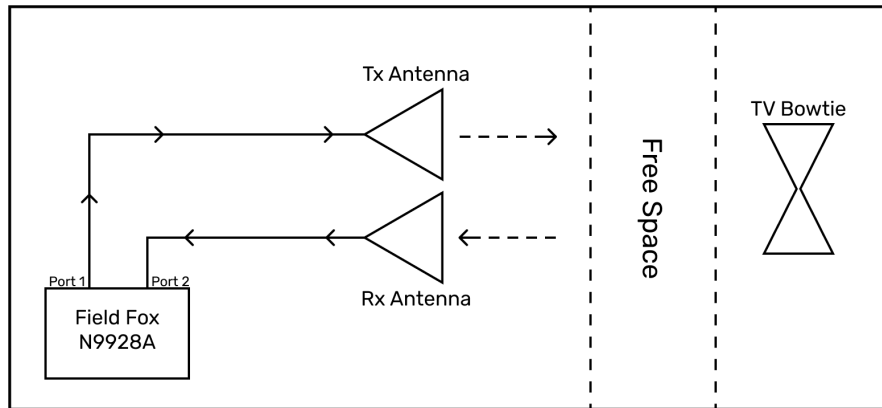
Figure 3.6: Block diagram of the physically symmetric monostatic system used to find the physically asymmetric system's receive chain losses.

The receive chain losses obtained using this approach were then compared to the cable loss in the receive chain's coax cable out of an interest to check the possible accuracy. The cable loss was expected to be the primary source of loss in the receive chain, so this quantity for the comparison. The comparison provided more confidence in the accuracy of the total receive chain loss measured using the physically symmetric system as the two measurements in Figure 3.7 showed close agreement across the frequency sweep.
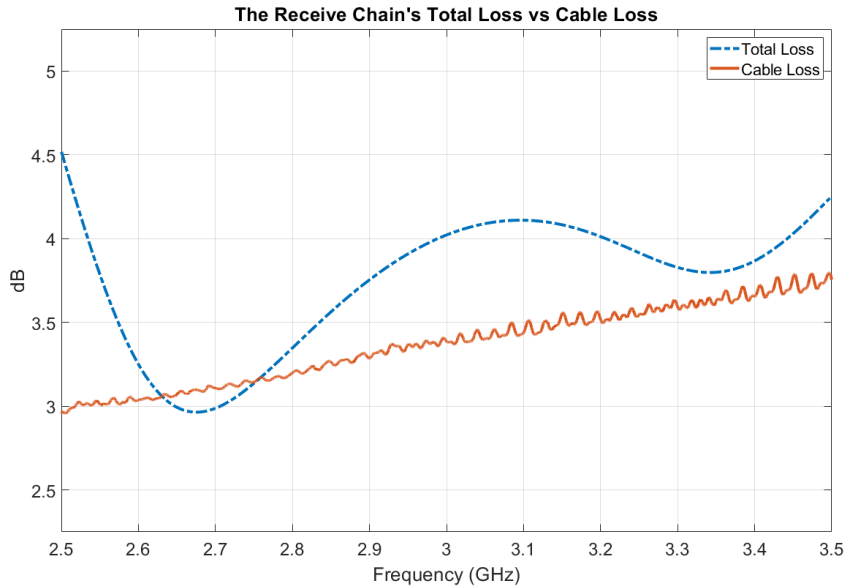
Figure 3.7: Comparing the cable loss of the coax used in the receive chain to the loss extracted from the symmetrical calibration factor.

Equipped with the receive chain's loss, the original asymmetric system's transmit losses were extracted. The resulting quantity shown in Figure 3.8 reports a negative amount of loss, which indicates gain. This outcome was expected due to the amplifier on the transmit chain. Notably, the amplifier offered, ideally, 19.5 dB of gain to the transmit signal.
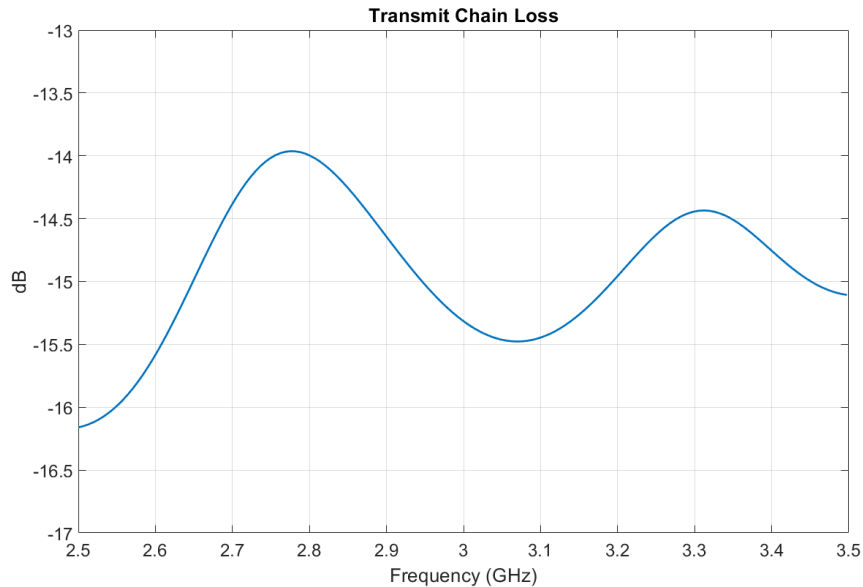
Figure 3.8: The monostatic radar's transmit chain loss across the frequency sweep

3.4 Cross-Frequency Electromagnetic Solvers

Due to the time-varying nature of the loaded antennas, conventional electromagnetic (EM) solvers could not be utilized due their LTI assumption. Many EM solvers operate under an LTI assumption and are thus not applicable for the desired cross-frequency simulations. Fortunately, a few EM solvers are capable of analyzing time-varying system behavior. The first solver is a hybrid of conversion matrices (CM) and method of moments (MoM) developed in-house [16]. The solver is able to quickly produce results thanks to its frequency domain approach, wherein "a time-varying system's response is described by the coupling between the voltages and currents at multiple frequencies" [16]. The second solver is XFdtd, a commercial-grade application of the finite difference time-domain (FDTD) algorithm [17]. At a high level, the FDTD algorithm operates by first discretizing a model into a mesh grid that divides the model into

tiny segments referred to as cells. The algorithm then determines the model's time-domain response by incrementally propagating fields through the system at a given time-stepping interval, thus allowing the program to analyze time-varying devices.

Modifications to XFdtd

Despite the apt use of XFdtd for the desired cross-frequency simulations, there were two limitations with the program's utility that were addressed during this thesis work. The first limitation addressed was that the program's method of creating time-varying circuit definitions was relatively inefficient. For example, in the case of a switch definition, every state transition had to be individually defined, requiring the user to set the time when each transition would begin, how long it would take, and the target state. As a solution, XFdtd's native scripting API was utilized to create a graphical interface, shown in Figure 3.9, that could be used to automate the creation of a switch definition. The GUI allows the user to define a switch with a particular transition frequency, number of cycles, rise/fall times, and duty cycle. The script then takes these parameters and defines a new definition automatically for the user.
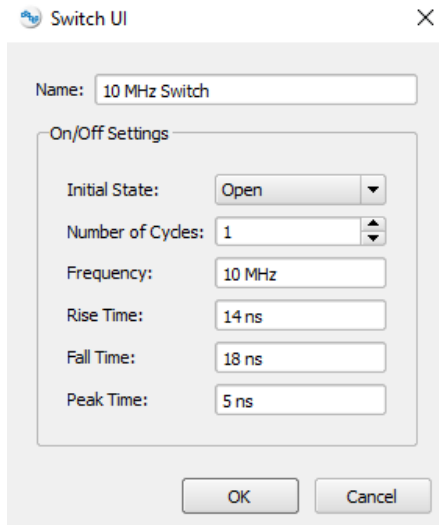
Figure 3.9: Switch Definition GUI used in XFdtd

The second limitation of XFdtd is that users are barred from recording far-field data when exciting their model with the program's native ramped sine wave. This restriction was a significant issue as the ability to record a time-varying structure's far-field performance when excited with a pure-toned signal was necessary. Unfortunately, there is no way to circumvent this restriction natively within the program, as Remcom sites an issue with detecting far-field convergence as the reason for this restriction. Fortunately, this restriction does not apply to user-defined waveforms. Thus, as a solution, a MATLAB script was developed that would generate ramped sinusoids and export them into a CSV file format, which could then be imported into XFdtd. An example of these ramped sinusoids is shown in Figure 3.10.
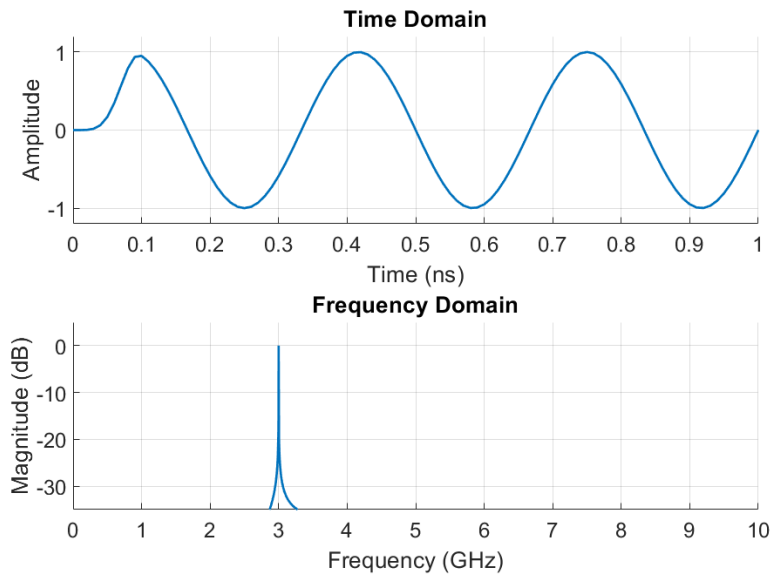
Figure 3.10: A 3 GHz ramped sine wave that was used to excite the time-varying scatters.

Chapter 4

Application and Validation of Cross-Frequency Backscatter

In the previous chapter, the term cross-frequency backscatter was introduced along with a set of procedures that could be used to quantify a time-varying DUT's scattering performance. This chapter will begin by introducing the bowtie antenna used for the cross-frequency measurements. Lessons and nuances to time-varying measurements gained during the cross-frequency measurement process are also presented. The techniques are essential in particular for producing consistent network analyzer measurements. Finally, the chapter concludes with the presentation of cross-frequency backscatter measurements along with comparisons to simulation results. The agreement between the measurements and simulation results provides credibility for methodology presented in this thesis.

4.1 Design and Fabrication of the Bowtie

Applying and verifying the methodology in the previous chapter required me to first design a time-varying scatter from scratch. A key feature the device was desired to exhibit was a wide bandwidth, as it would maximize the number of harmonics that could potentially scatter off of the device. Another possible feature of interest was for the structure to be non-directional to help minimize the possibility of poor alignment

between the DUT and the radar system causing disagreement between measurements and simulations. One classical antenna design that meets these needs is the bowtie antenna.

The bowtie antenna, sometimes called the butterfly antenna, is a modified form of the classic half-wavelength dipole, offering a broader bandwidth performance due to the sides of the structure fanning out in a radial fashion, shown in Figure 4.1 [18]. This increased physical area allows for more frequencies to reside along the metallic surface. Still like the half-wave dipole, the bowtie's end-to-end length will still play a part in determining the operating frequencies. However, the structure's total frequency range also depends on the angle between the two fanned sides [18]. By decreasing the angle "D", the structure's bandwidth will decrease. A bowtie antenna with a side to side angle D of zero is simply a dipole. The average bowtie antenna will exhibit a radiation pattern resembling the doughnut pattern of the half-wave dipole due to their similar geometry. The bowtie's peak in its radiation pattern is located normal to the antenna's face and centered above the middle of the structure. As shown in Figure 4.1, The unloaded bowtie structure was designed to offer a VSWR less than three for 500 MHz and centered on 3 GHz.
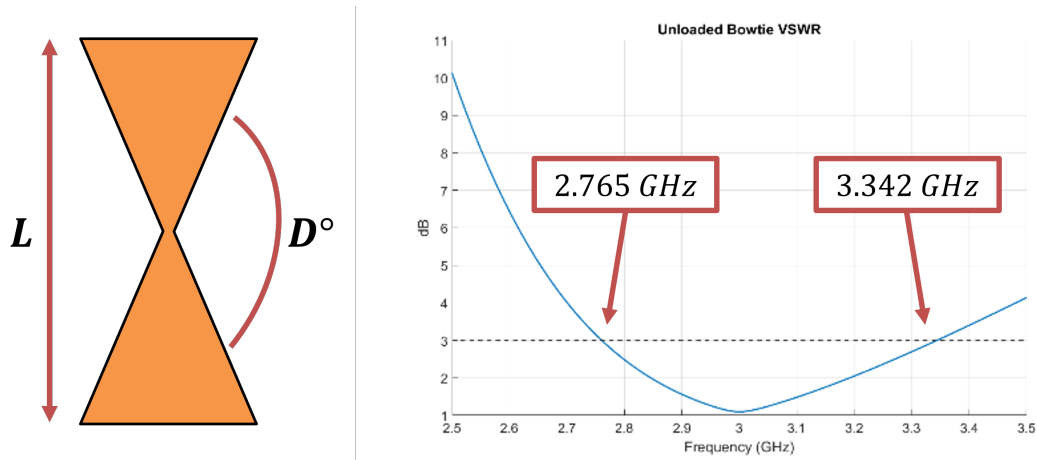
Figure 4.1: Model and picture of the 3 GHz tuned bowtie used as my time-varying scatter

4.1.1 The Switch Loads

The switches used as the TV loads are the Analog Devices absorptive (ADG901) and the reflective (ADG902) radio frequency(RF) switches. The schematics for both switches are shown in 4.2, wherein on top of the primary switching circuitry, the reasons for the absorptive and reflective tags can also be seen. In the case of the 901, two 50 ohm loads are used to ground each RF terminal via grounding switches. The grounding switches are inverted to the main switch located between the RF channels. Assuming impedance matching, when the 901 switch is in its "open" state, the RF channels will be grounded the 50 ohm loads to minimize power reflecting off the main switch's "open" terminals. The 902 model features a single ground switch, which when the main switch is "open" shorts to ground only the second RF channel. The first RF channel is then left floating, allowing any power residing on that channel to reflect off the main switch's open terminals.

ADG901

ADG902

Figure 1. ADG901
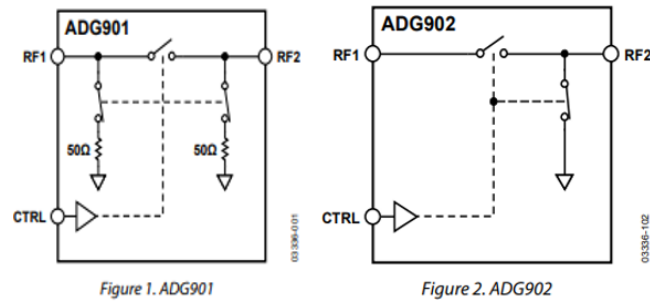
Figure 2. ADG902

Figure 4.2: Schematic diagrams, respectively, of the ADG901 and ADG902 switches

Integrating these switches into my bowtie design required me first to create a gap in the center of the structure wide enough to fit the small package. The switch was then rotated so that the switch's RF channels would be lined up with the two bowtie halves, ideally minimizing the switch's impact on the structure's performance. Trace lines were then added to carry the switch's DC power, ground, and control signals. These traces extend to the board's edge and connect to a four-pin header during the fabrication process. Notably, a fourth trace only extends about halfway onto the board from the pin header. This fourth trace is a ground line added to ease the process of attaching the biasing network components that connect the power line and ground.
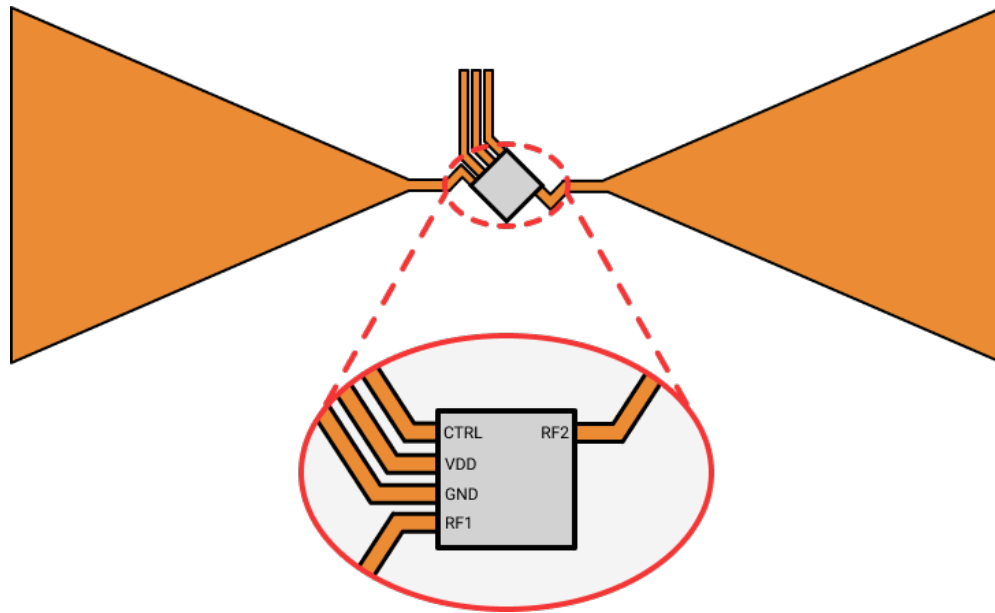
Figure 4.3: The bowtie design updated with trace lines that integrate in the RF switch.

4.1.2 The Fabrication Process

The bowtie was printed onto a Rogers 3203 substrate board with a material thickness of 0.55 millimeters and a dual sided electrically deposited 1 ounce copper layer. The 3203 substrate was chosen due to the material's low permitivity ($\varepsilon_r =$???), which was intended to minimize the potential impact on the antenna's radiation performance. The substrate also offered a unique material makeup that included no fiberglass, allowing for the board to be exposed to higher levels and longer duration of heat.

The bowtie was etched from the board's copper layer using the LPKF U4 laser etching machine. This machine was chosen for the job as it is capable of high-resolution circuit board prints, offering a resolution of 2 mil lines and spaces. Unfortunately, due to the board's thicker deposit of copper, one ounce, the board would often require multiple cycles through the system's heating and hatching sequences to thoroughly remove the layer of copper from the substrate. The default number of cycles the machine rec-

ommended was four hatching and only one heating sequence. Ten to twelve hatching cycles and at least two heating sequences were found to be ideal for thoroughly removing the copper layer. A comparison between results obtained using the default and the more optimal settings is shown in Figure 4.4. The need for multiple runs through the laser etching sequence was why a board with a high heat tolerances was required. A board with fiberglass woven into its material makeup would easily burn during multiple laser exposures.
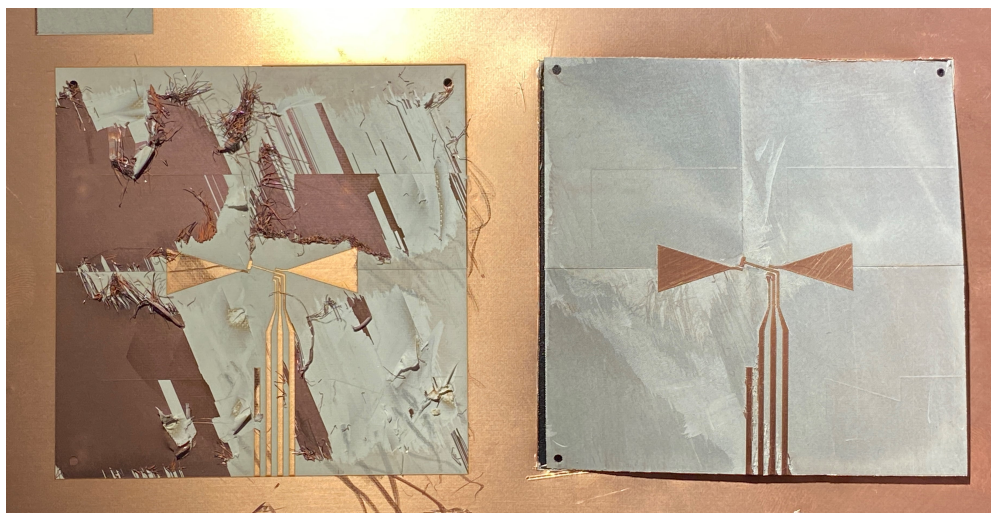
Figure 4.4: Comparing the outcome of printing the bowtie using the default etching settings against my modified settings.

4.1.3 The Switch Control Network

The switches were powered via a twin lead feed that would supply the 2.75 volts from a DC power supply located at the foot of the antenna under test (AUT) mounting pedestal. The control signals were supplied to the switch from a signal generator via a 50-ohm coax cable that transformed into twisted pair near the DUT. Figure 4.5 shows how this feeding network looked when set up in the far-field chamber.
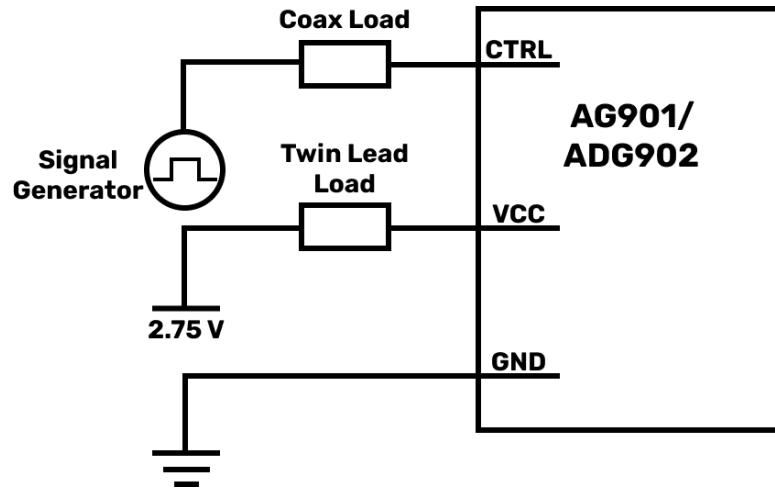
(a)
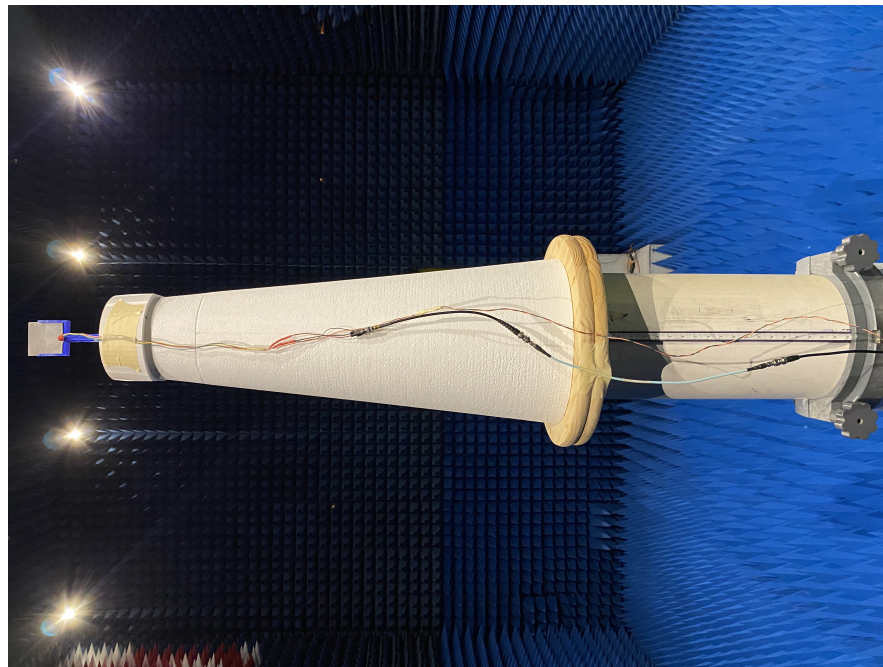
(b)

Figure 4.5: (a) Diagram and (b) photo of the circuitry used to control the time-varying loads.

4.1.4 Measurement Setup

As Figure 4.6 shows, the field fox was placed inside the chamber at the base of the radar's pedestal so that the door could be fully shut. The field fox was controlled automatically via a LabView script running on the laptop shown in Figure 4.6. The inclusion of the laptop and field fox inside the chamber could be a source of error in the measurements that will presented in a later section. However, this possible error is considered to be minuscule.
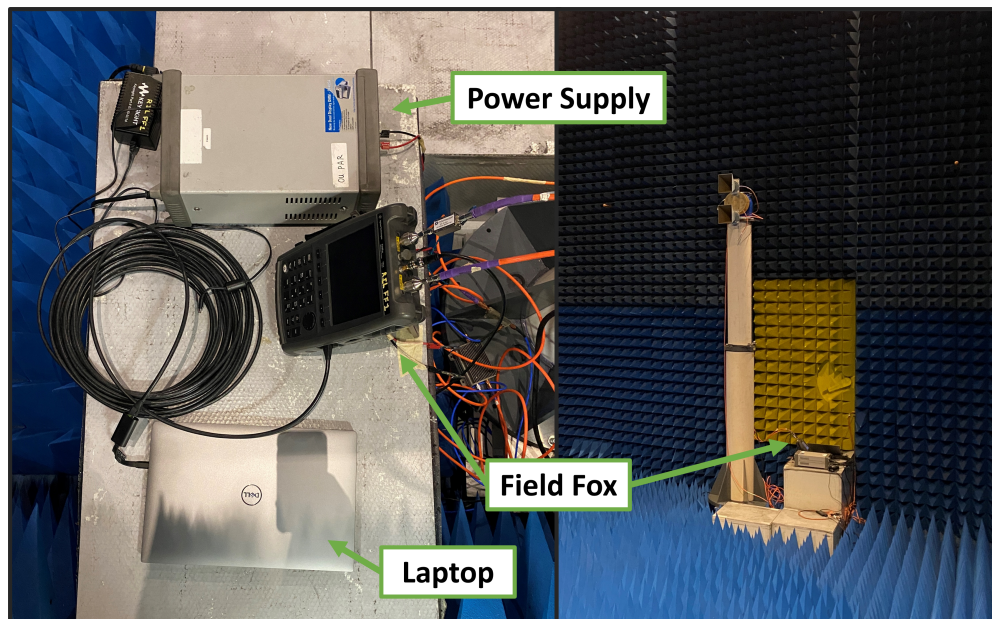
Figure 4.6: Picture of the radar setup inside the chamber.

4.2 Consistency with Network Analyzer Measurements

Initially, there were consistency issues with the time-varying bowtie's S_{21} measurements, this issue is highlighted when comparing the measurements in the frequency-domain. As Figure 4.7 shows, two S_{21} measurements could be taken a day apart, and despite the antenna's position being constant, the target's response would change

dramatically across frequency. It turns out that this was an issue with the measurement's temporal resolution being too coarse, leading to the scattering responses from the bowtie and the control circuitry being lumped together into the same time bin. The bowtie and twin leads being lumped together lead to inconsistencies between measurements due to the twin leads failing to capture and re-radiate the same amount of power each time. The issue was resolved by increasing the frequency sweep from 2.5 - 3.5 GHz to 2 - 4 GHz, which in turn doubled the temporal resolution allowing for the time-varying bowtie's response to be isolated from random reflections off the load wiring.

Figure 4.7: The early S_{21} measurements had a temporal resolution that was too coarse, leading to consistency issues.

4.3 Cross-Frequency Backscatter Measurements

The following section presents cross-frequency backscatter measurements of two antennas, one loaded with the absorptive ADG901 switch 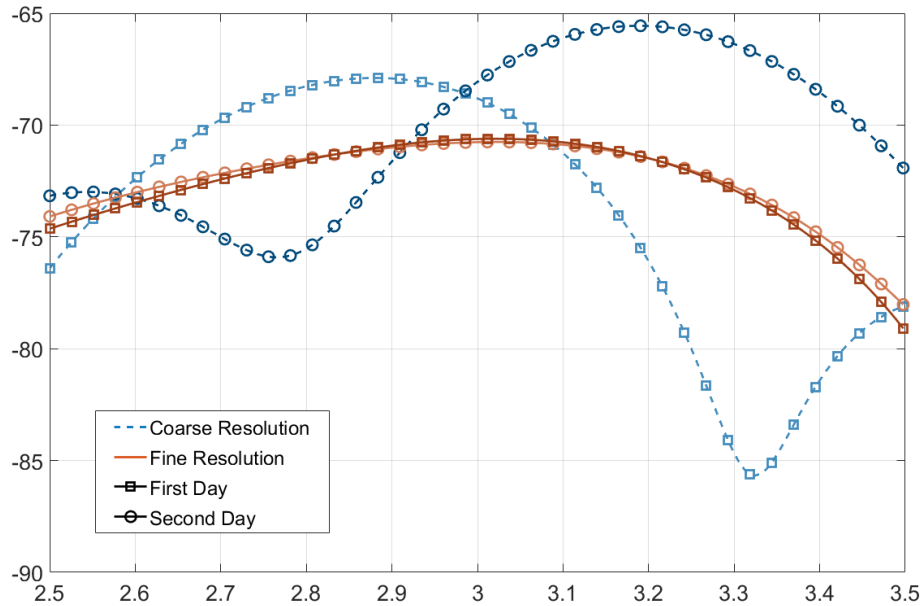and the other loaded with the reflective ADG902. The devices were both excited at 3 GHz and their responses were measured from 2.8 to 3.2 GHz. Both antennas' backscatter is measured while their loads operate at four time-varying frequencies, 4, 5, 10, and 20 MHz. Two time-invariant control cases are also provided, one with the switch "open" and one with the switch "closed". The measurements are supported through comparison to simulation results. The comparisons show ample agreement between the three data sets. The few differences between the data sets are addressed, and identified as likely resulting from the switches' time-domain behavior.

4.3.1 The Absorptive Switch

The most notable agreement was found regarding the location of harmonics and their trend in magnitude moving away from the incident response. In Figures 4.8, 4.9, 4.10, and 4.11 the measurements and simulation results can be seen reporting agreement on the magnitude of the incident response and the first two odd harmonics. In Figures 4.8 and 4.9 the high level of agreement between the datasets on the odd harmonics extends to even higher-order odd harmonics at those lower time-varying frequencies. The more significant agreement could result from those lower frequencies residing more within the switch's range of operation. While the higher time-varying frequencies, 10 and 20 MHz, do not exceed the switch's upper limit of 100 MHz, they do come closer [19]. The comparisons show that all three datasets agree on the presence of the even harmonics, but not always on their magnitude. The disagreement could have resulted from the even harmonics being close to the noise floor, primarily in the time-varying cases 4 and 5

40

MHz.

In all four time-varying cases, there is a disagreement between the datasets regarding the symmetry of the harmonics about the excitation frequency. The measurements report significant asymmetry, which seems to increase at higher-order harmonics. In contrast, XFdtd and CM-MoM report minimal asymmetry on the order of less than 0.5 dBsm. The measurement asymmetry is most significant in Figure 4.11, and is likely a result of the switch's physical limitations or fabrication error. For two reasons, the measurement process has been concluded as not the source of the asymmetry. First, the uncalibrated scattering measurements also report the asymmetry. Second, an evaluation board will also report an asymmetric spectrum when a 3 GHz signal is applied to the switch's RF channels. An example of this evaluation board's asymmetry is seen in Figure 4.12. Finally, there was an idea that the asymmetric harmonics resulted from the bowtie having an asymmetric resonance around 3 GHz. This idea originates from recognizing that most of the harmonics below 3 GHz are higher than those above. While the bowtie was found to have an asymmetric resonance around 3 GHz, its peak is shifted slightly above 3 GHz, as shown in Figure 4.13. This finding meant that an asymmetric resonance could not be the source of the asymmetric harmonics.

It is also concluded from these measurement comparisons that polyharmonic distortion is either non-existent or minimal in the measurements. In [20], the concept of amplifiers producing polyharmonic distortion is addressed, and this phenomenon was of concern due to the field fox's receive amplifier. However, because the simulations and measurements show such significant agreement, it is concluded not to be an issue. If this phenomenon had a significant impact on the measurements, then the measurements and simulations would not agree since XFdtd and CM-MoM were not modeling that effect. If one desired to further confirm the minimal impact of polyharmonic distortion, they could retake the measurements twice. The first retake could keep the Field

Fox's internal attenuation set to 0 dB, and the second measurement could have the attenuation set to any other value. If those two measurements have backscatter with equal magnitude, then it confirms polyharmonic distortion is not a significant issue.
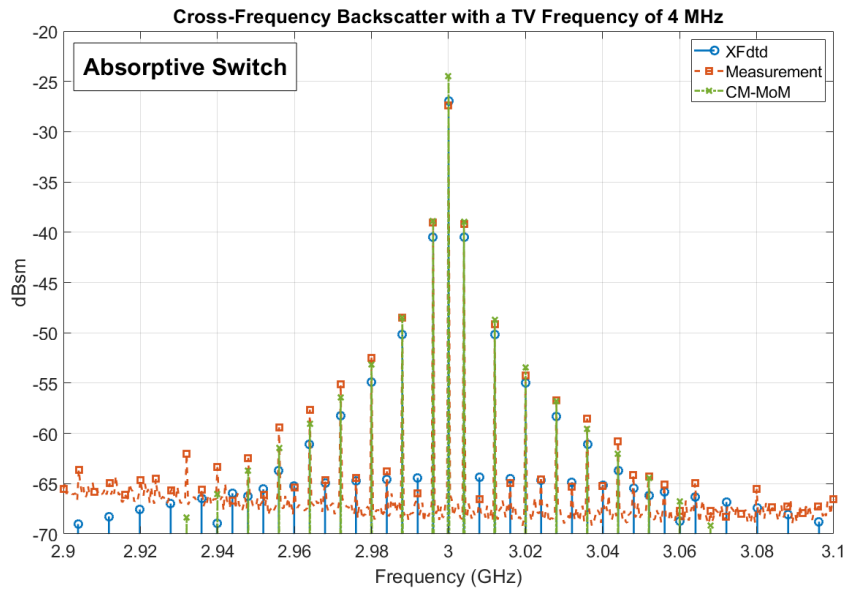

Figure 4.8: Cross-Frequency backscatter of the Bowtie while the absorptive switch opens and closes at a rate of 4 MHz.

Figure 4.9: Cross-Frequency backscatter of the Bowtie while the absorptive switch opens and closes at a rate of 5 MHz.
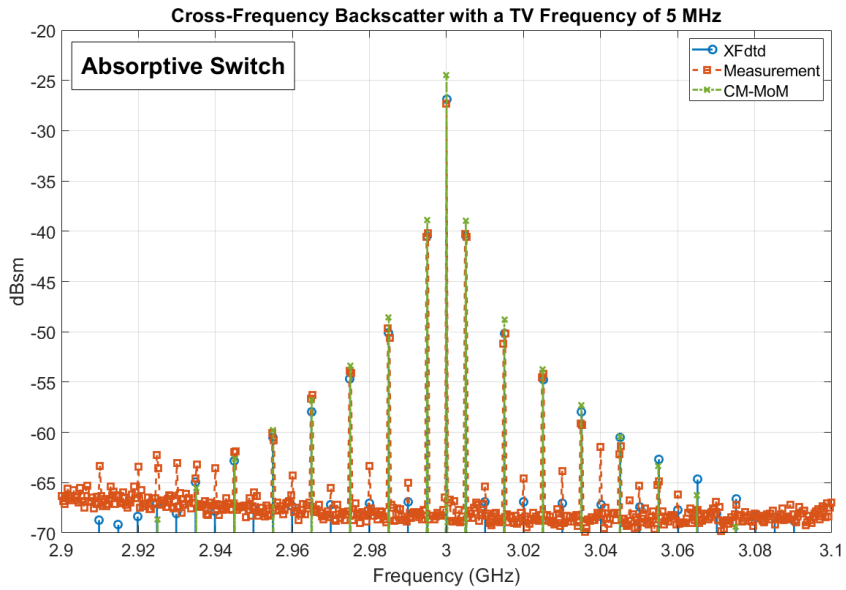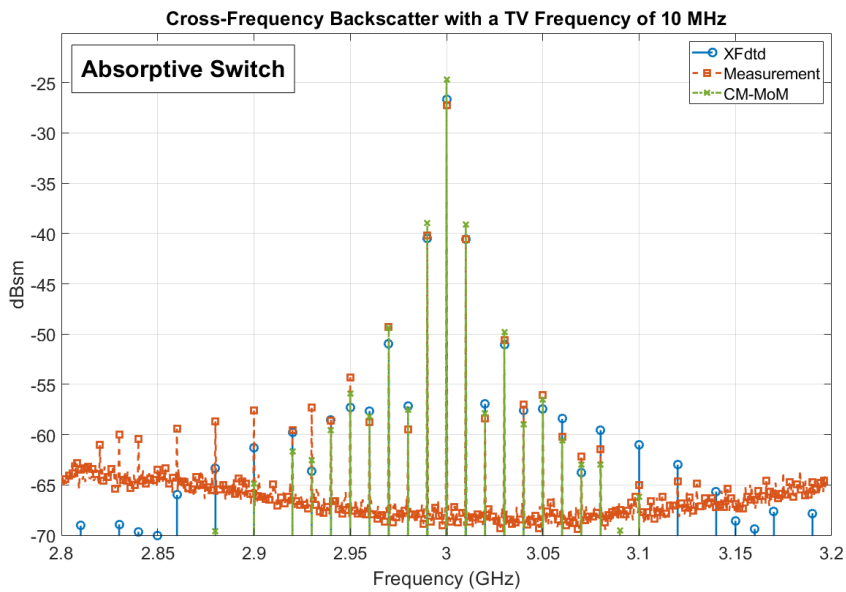

Figure 4.10: Cross-Frequency backscatter of the Bowtie while the absorptive switch opens and closes at a rate of 10 MHz.
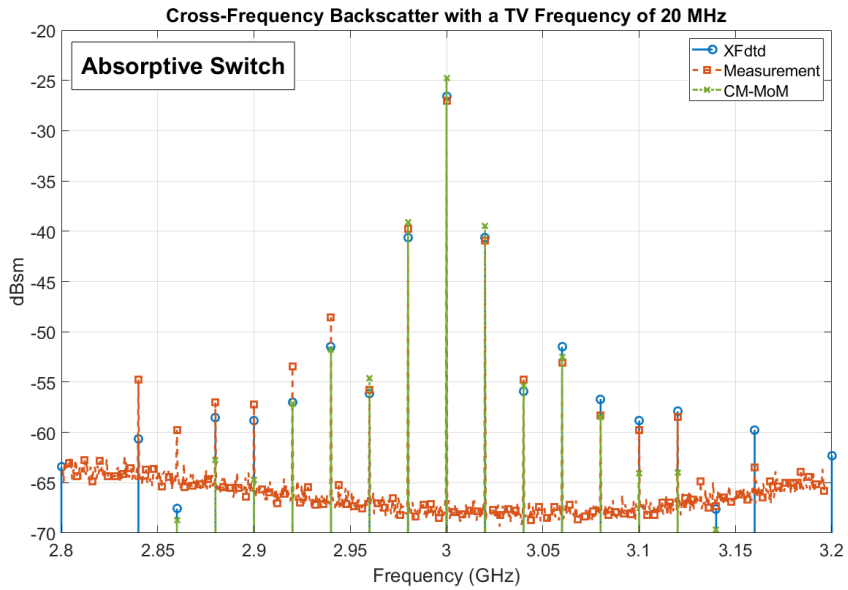
43

Figure 4.11: Cross-Frequency backscatter of the Bowtie while the absorptive switch opens and closes at a rate of 20 MHz.
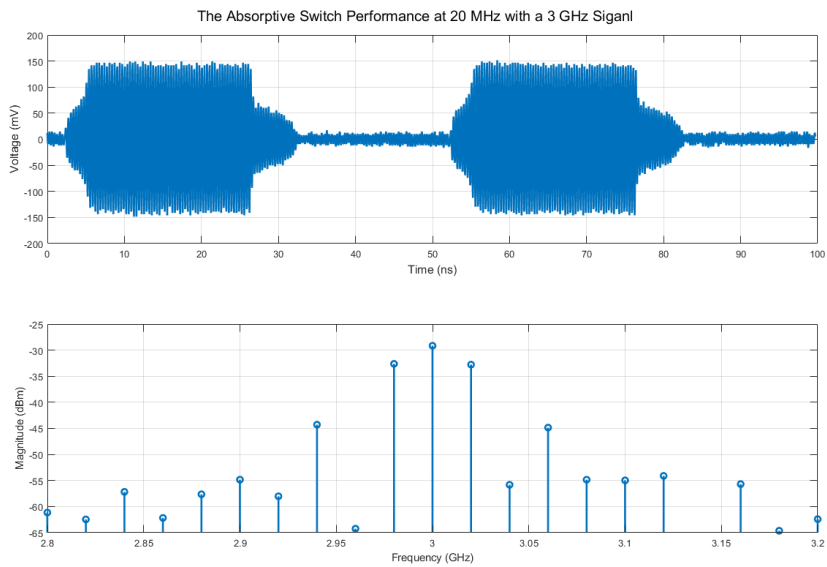

Figure 4.12: A 3 GHz signal modulated by the ADG901 switch operating at 20 MHz on an evaluation board.
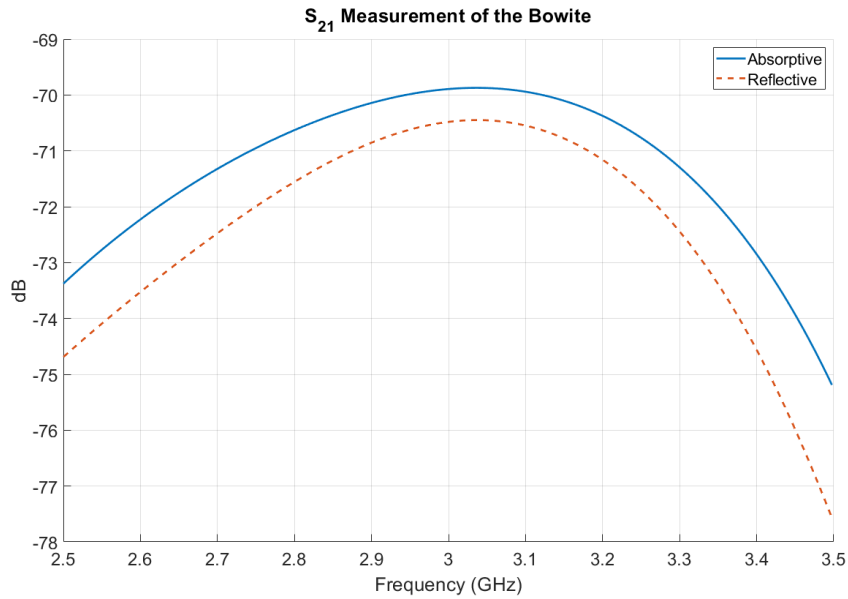
Figure 4.13: Standard S_{21} measurement of the bowtie loaded with the absorptive switch and reflective switches showing that the scatter experiences a peak resonance above 3 GHz.

4.3.2 The Reflective Switch

The cross-frequency backscatter measurements of the bowtie loaded with the reflective ADG902 switch showed ample agreement to the respective simulation results. Similar to the measurement and simulation comparisons with the absorptive switch, the most notable agreement seen in Figures 4.14, 4.15, 4.16, 4.17 is on the location of harmonics and their trend in magnitude as the order increases. The measurements and simulations agreed within 1.5 dBsm of each other on the incident response and first two odd harmonics. Additionally, there was agreement on the existence of the even harmonics, but there was still disagreement on the magnitude.

Like the absorptive cases, the reflective measurements report asymmetry in the harmonic generation, especially at higher time-varying frequencies. Additionally, this

trend was once again not as prevalent in the simulations. The source of this observed asymmetry is still believed to result from the asymmetry in the switch's performance.

Figure 4.14: Cross-Frequency backscatter of the Bowtie while the reflective switch opens and closes at a rate of 4 MHz.

Figure 4.15: Cross-Frequency backscatter of the Bowtie while the reflective switch opens and closes at a rate of 5 MHz.
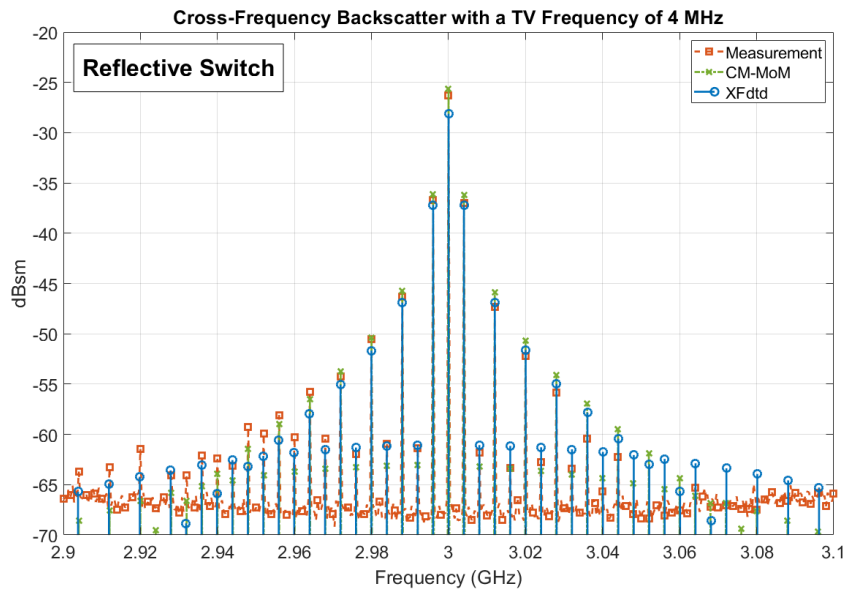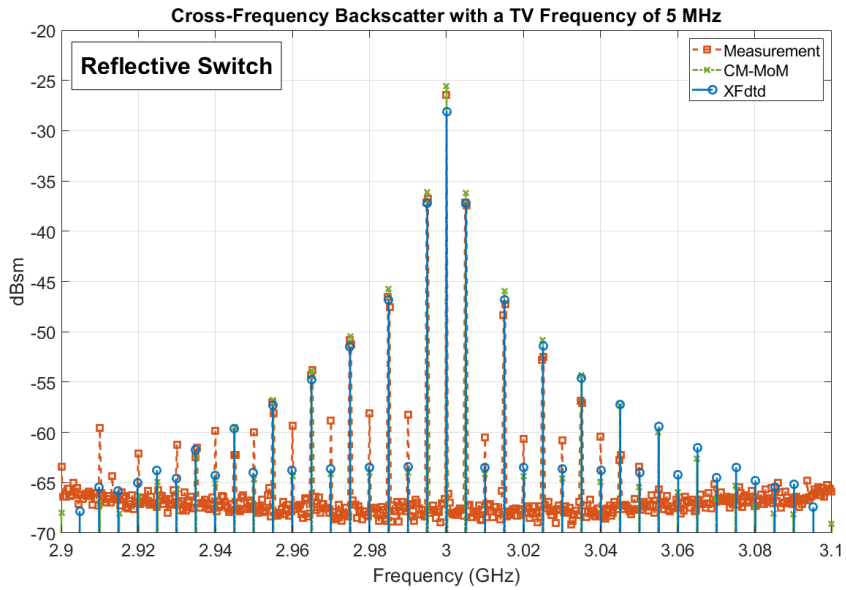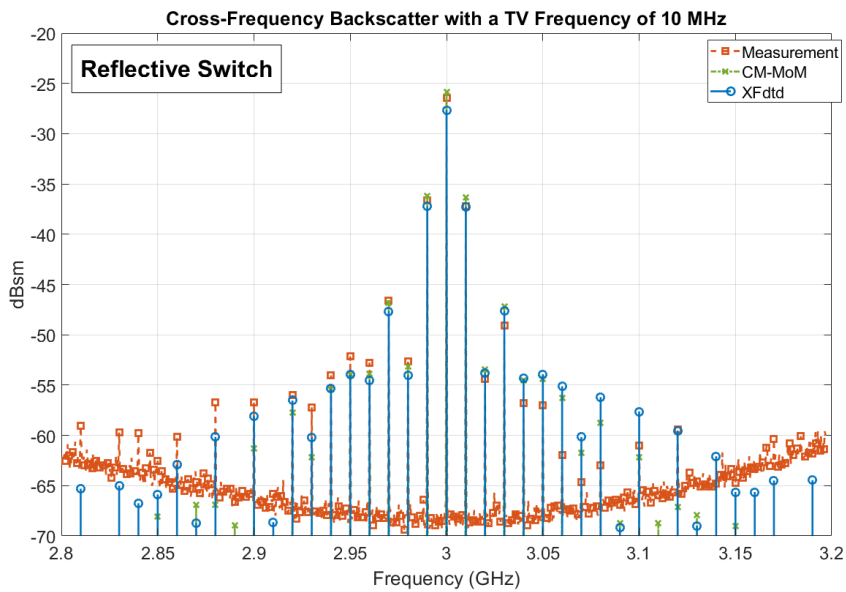

Figure 4.16: Cross-Frequency backscatter of the Bowtie while the reflective switch opens and closes at a rate of 10 MHz.
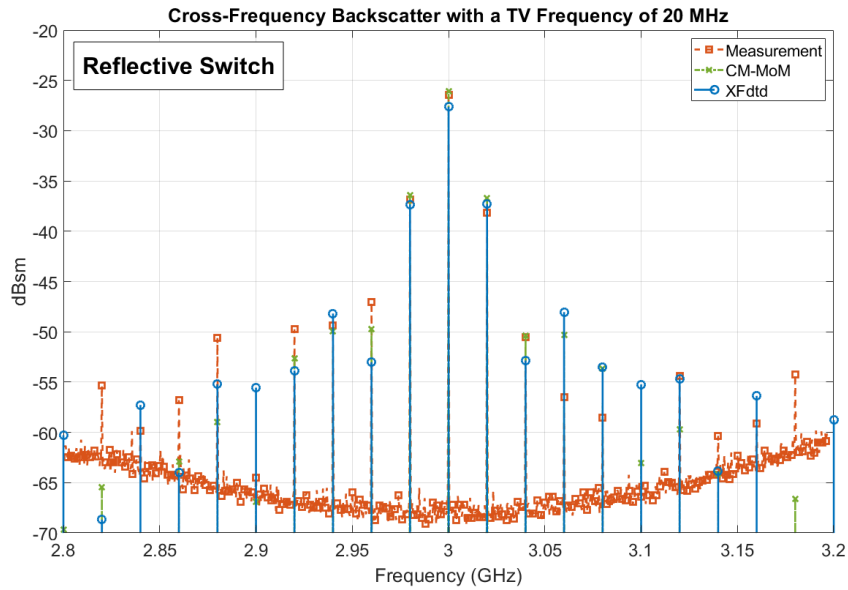
Figure 4.17: Cross-Frequency backscatter of the Bowtie while the reflective switch opens and closes at a rate of 20 MHz.

4.4   Supporting Measurements with Simulations

Producing the simulation results that supported the cross-frequency backscatter measurements required careful consideration of the antenna's physical structure and the time-domain behavior of the 901 and 902 switches. As figure 4.18 shows, two trends were identified in the cross-frequency backscatter measurements that were believed to be produced by different aspects of the switch's time-domain performance. The first trend was the relationship between the excitation frequency response and the first harmonic. specifically, the ADG901 measurements reported a 13 dBsm difference between the incident and first harmonic, and the 902 measurements reported a 10 dBsm difference. The second trend was the amplitudes of the even and odd harmonics relative to each other. In the slower time-varying frequency measurements of 4 and 5 MHz, the

amplitudes of the even and odd harmonics showed greater differences in magnitude. In contrast, the faster pumping frequency measurements of 10 and 20 MHz produced even and odd harmonics with magnitudes closer to each other.
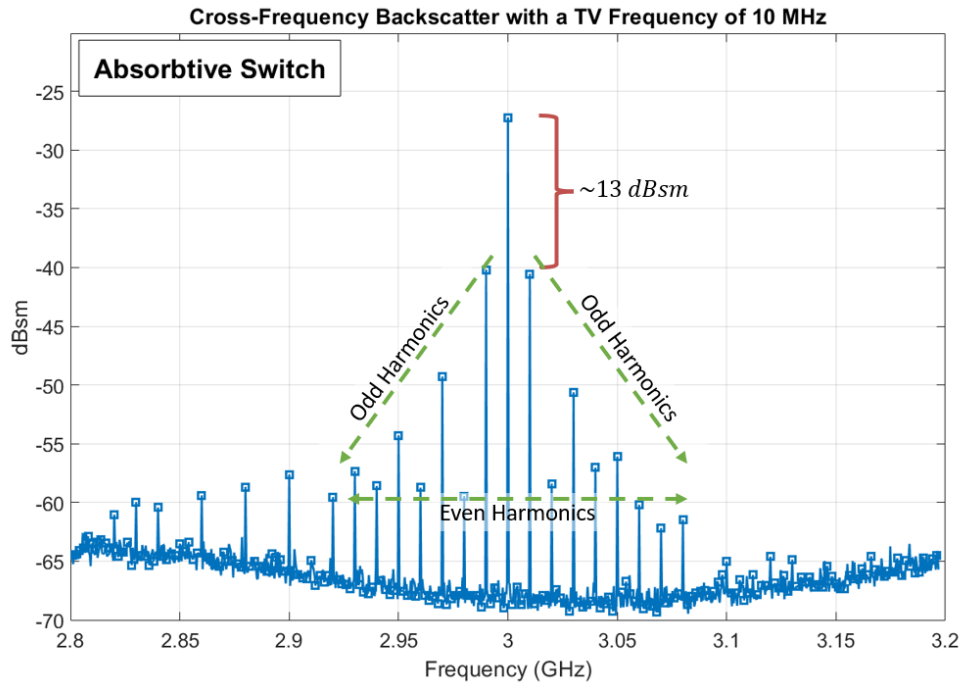
Figure 4.18: Identifying two trends in the 10 MHz cross-frequency backscatter measurement that are were of interest during the modeling process.

To aid the investigation of these spectra relationships, the switches were initially modeled using an ideal square wave that transitioned from an ideal open and close. Utilizing this modeling approach offered a convenient and efficient method for identifying the sources of the two trends identified in the measurements. The model presented in Figure 4.19 uses 10 MHz as the time-varying frequency because the shape of the 10 MHz measurement's spectrum was in between the spectrum seen in the 4, 5, and 20 MHz measurements. The final switch model shown in this Section was the model used in the electromagnetic solvers XFdtd and CM-MoM to generate the results shown in

Section 4.3.

4.4.1   The Even and Odd Harmonic Relationship

Ideally the transition between an opened and closed state is instantaneous, and assuming that the switch flips between states at a rate of 10 MHz with a duty cycle of 50 percent, it will produce a time-domain pattern and frequency spectrum like the one in Figure 4.19.
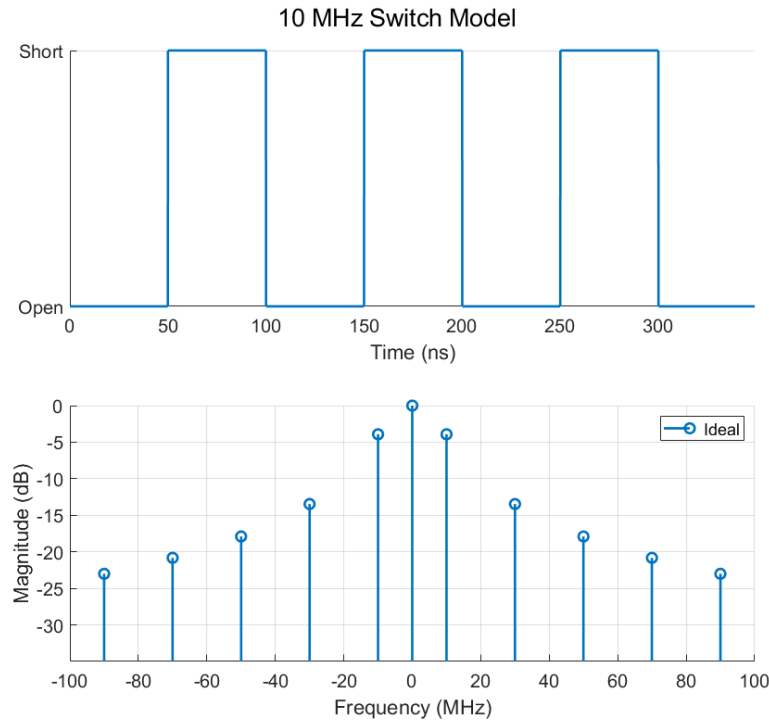

Figure 4.19: Model of an ideal switch operating at 10 MHz with a duty cycle of 50 percent.

The switches used in my measurements are non-ideal, which means they require some time to transition between states. Fortunately, these transition times are provided in the ADG901 and 902's datasheet. During typical operation, both switches require 5

nanoseconds to transition to a short, and 8 nanoseconds to transition to an open [19]. As shown in Figure 4.20, if these realized transition times are implemented into the model, it introduces even harmonics into the signal's frequency spectra.

Figure 4.20: Model of a non-ideal switch operating at 10 MHz with a duty cycle of 50 percent and opening/closing times of 8/5 nanoseconds.

The final step for reproducing the even and odd harmonic relationships was considering the likelihood of the real switches not operating at the intended 50 percent duty cycle. Unfortunately, there is no discussion on this idea included in the switches' datasheets, but after testing several duty cycles near 50, a value of 47 percent produced the desired even and odd harmonic relationships, as seen in Figure 4.21.

Figure 4.21: Model of a non-ideal switch operating at 10 MHz with a duty cycle of 47 percent and opening/closing times of 8/5 nanoseconds.

4.4.2 The Incident and First Harmonic Relationship

The second trend observed in the backscatter measurements was identified as the result of the switch's non ideal short and open states producing a non-ideal average value. A signal's average value, or DC component, is determined by the normalized area under the signal for one full period [21],

$$AV = \frac{\int_0^T f(t)\,dt}{T}\ .\tag{4.1}$$

In Figure 4.21, the model was made assuming that the switch transitioned between an ideal short and open. However, as Figure 4.22 demonstrates, the signal's average

52

value increases if the switch transitions between an ideal short and a non-ideal open. The increase to the average value leaves less energy available to the harmonics, producing the incident and first harmonic relationship seen in the backscatter measurements while maintaining the even and odd harmonic relationship.
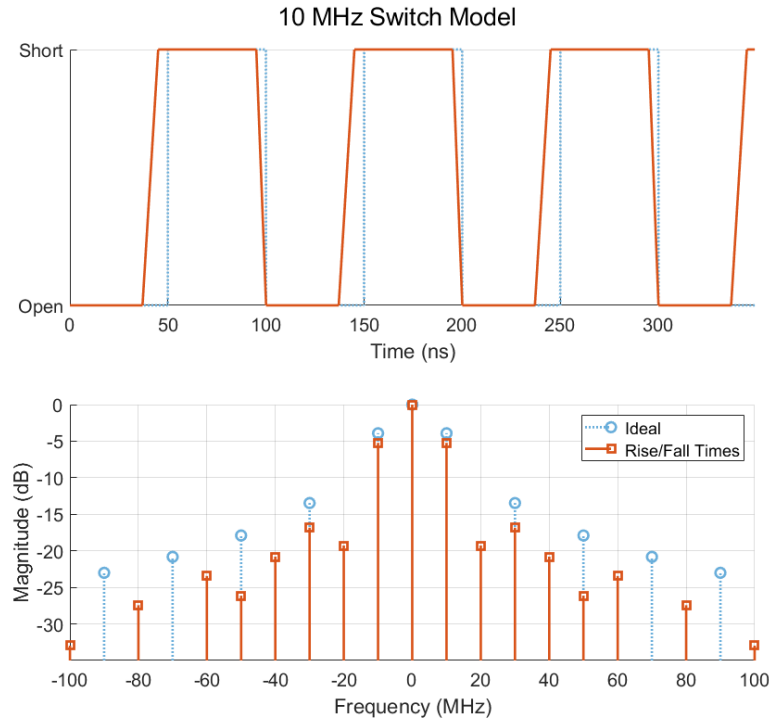

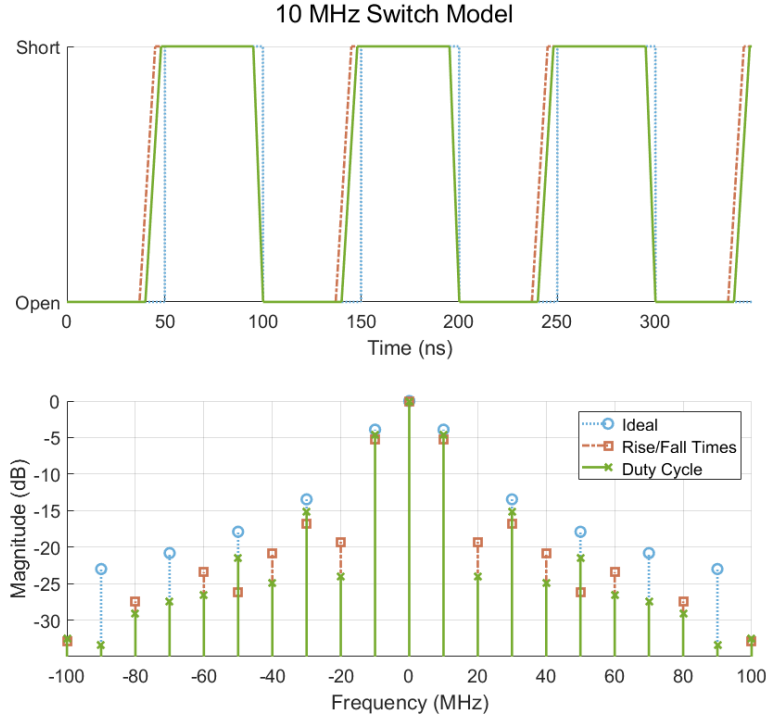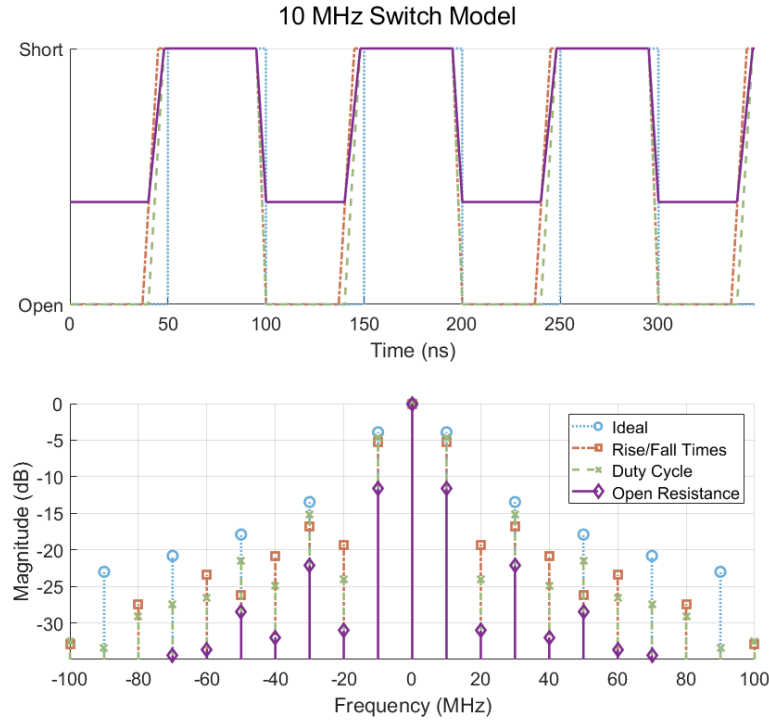Figure 4.22: Model of a non-ideal switch operating at 10 MHz with a duty cycle of 47 percent and opening/closing times of 8/5 nanoseconds. Transitioning between an ideal short and a non-ideal open, thus increasing the signals average value.

This switch model shown in Figure 4.22 was implemented into XFdtd and CM-MoM to generate the simulation results shown in Section 4.3.

Chapter 5

Cross-Frequency Effective Aperture, Methodology, and Application

In the previous chapter, the capabilities of the cross-frequency backscatter measurement methodology was demonstrated via comparisons between measurements obtained following procedures and simulation results. The comparisons showed ample agreement between the two datasets under a variety of cases. This chapter focuses on a new cross-frequency form of effective aperture, which will describe the power received at several frequencies when a single tone is transmitted. A measurement process for cross-frequency effective aperture is laid out and applied to a modified form of the bowtie introduced in Chapter 3. The cross-frequency measurements are then compared to simulation results.

5.1   Introduction to Cross-Frequency Effective Aperture

In standard practice, one would turn to the quantity of Gain to describe an antenna's ability to capture power. However, the term gain is not applicable for a time-varying radiator as the term's definition involves a reciprocity assumption [18]. Fortunately, the term effective aperture also quantifies the power captured by a radiator but is free of any LTI assumptions. Effective aperture is explicitly a receive term, used to describe the ratio of power that an antenna effectively captures in any direction to the transmitted

power density and the Gain of the transmitter,

$$A_R = \frac{P_R 4\pi R^2}{P_T G_T} \; .$$ (5.1)

The expression of effective aperture is evaluated at just the incident frequency in a measurement. The incident frequency restriction prevents the expression from capturing a time-varying antenna's expected harmonic generation. The assumption was then broken, and Equation Eq. (5.2) is modified to capture and normalize the behavior of interest forming cross-frequency effective aperture. Cross-frequency effective aperture expresses the power received across multiple frequencies at any direction to a pure-toned transmitted power, radiated by an antenna with a known gain,

$$A_R(f_i, \vec{f_j}) = \frac{P_R(\vec{f_j}) 4\pi R^2}{P_T(f_i) G_T(f_i)} \; .$$ (5.2)

5.2 Cross-Frequency Effective Aperture Methodology

The measurement setup for my effective aperture measurements, shown in Figure 5.1, carries over some equipment from the scattering section of this thesis. Most notably, the transmit chain still includes the 20 dB amplifier to ensure that the incident wave has an SNR high enough when it reaches the time-varying bowtie. The same field fox model was again used, as the cross-frequency effective aperture measurements required spectrum data. Finally, the same S-band horn antenna was used on transmit. The setup differs from the monostatic setup in regards to the cabling, as Figure 5.2 shows. This setup takes advantage of the chamber's bulkhead to connect the transmit antenna and bowtie to the field-fox's first and second ports, respectively. Notably, the cable loss in the system was higher than the monostatic system due to the use of the bulkhead, which

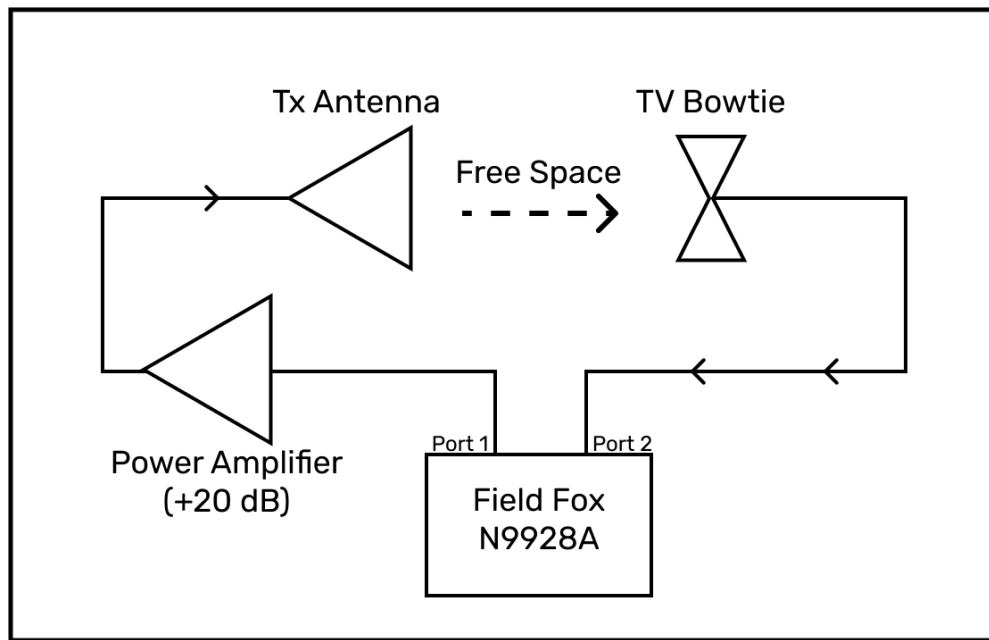is additional reasoning for keeping the amplifier on the transmit chain.

Figure 5.1: Diagram of the chamber setup used for the cross-frequency effective aperture measurements.
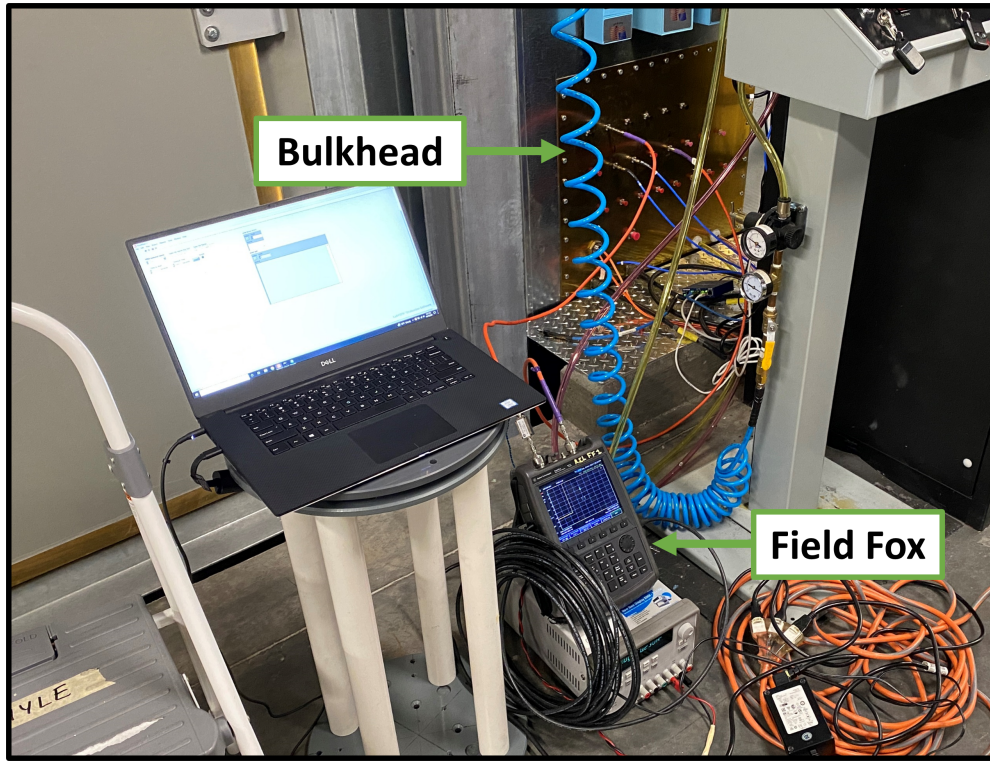
Figure 5.2: Picture of the field-fox connected to the bulkhead

The process of taking a cross-frequency effective aperture measurement is outlined in Figure 5.3 and begins by introducing a pure-toned signal via a plane wave excitation into the chamber setup in Figure 5.1. This incident wave will then induce a current along the surface of the time-varying bowtie, which the switch will then modulate. This modulated signal's frequency content is recorded using the spectrum analyzer mode of the field-fox. The spectrum measurement provides the received power measurement, which is calibrated to cross-frequency effective aperture using the effective aperture calibration term, K_A. Notably, the cross-frequency effective aperture methodology requires no multipath compensation, and only the spectrum measurement as multipath signals are not of concern as the setup and nature of the measurement removes the impact of coupling and reflections.
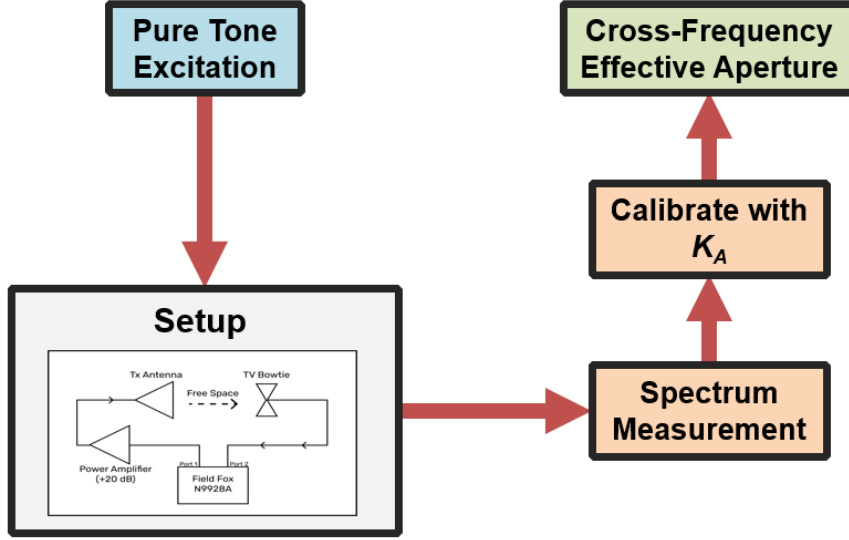
Figure 5.3: The general process of taking a cross-frequency effective aperture measurement

5.2.1 Effective Aperture Calibration Factor

The cross-frequency effective aperture calibration factor is comprised of three terms, two of which are constant across frequency and already known. The realized gain of the transmit antenna at the excitation frequency is the unknown frequency-dependent term and must be obtained from a calibration measurement. A calibration measurement replaces the DUT with an antenna equipped with a known gain. The calibration antenna in this experiment was another Narda S-band horn antenna, and the transmit realized gain is expressed as,

$$G_t = \frac{P_r 4\pi R^2}{P_t G_r G_a \lambda^2} \; .$$ (5.3)

The gain of the transmit antenna across the receive frequencies is shown in Figure 5.4. However, only the value at the excitation frequency of 3 GHz is needed to extract

cross-frequency effective aperture. The system's loss across frequency is extracted from the realized gain and shown in Figure 5.5. The loss in the system shows expected behavior across frequency and reports an expected magnitude.
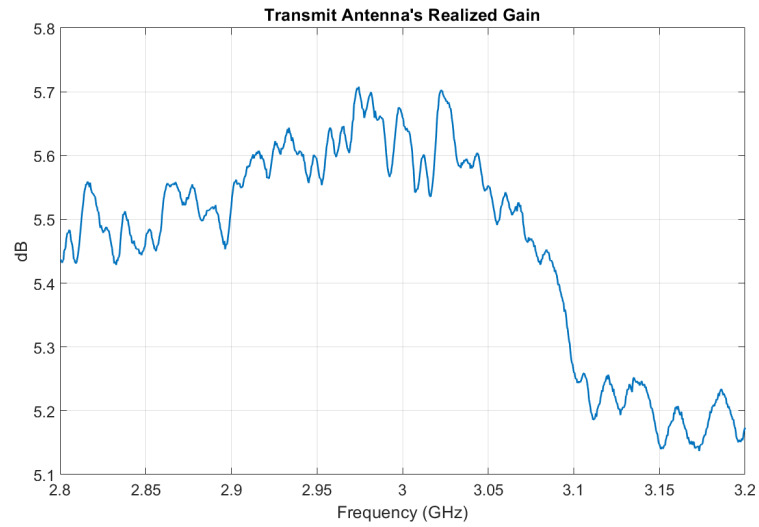

Figure 5.4: The realized gain of the NARDA S-band horn antenna used on transmit.
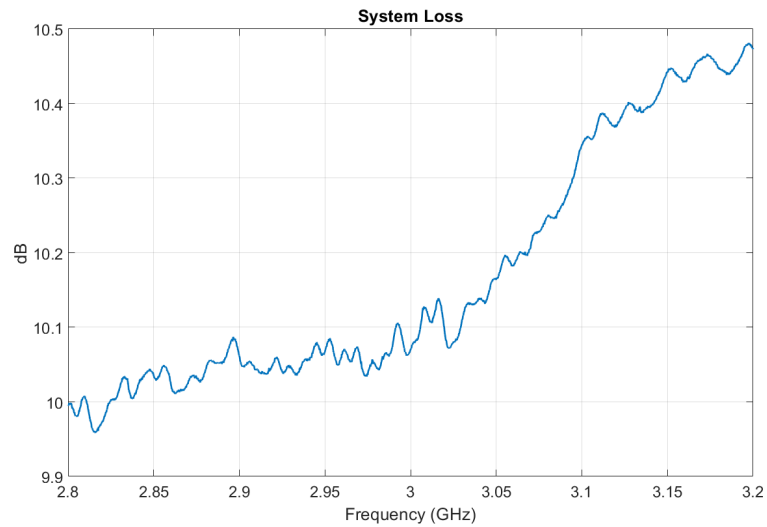

Figure 5.5: The system loss resulting from missmatch inefficiencies and attenuation.

5.3   Updating the Bowtie for Received Power Measurements

Applying the cross-frequency effective aperture methodology required a time-varying antenna loaded with an RF connector capable of delivering the power captured by the antenna to the field fox. A modified form of the bowtie utilized for the scattering measurements in Chapter 4 was used for the experiment. The bowtie was loaded with a twin-lead line that connected the two halves of the bowtie to a coax cable, as shown in Figure 5.6. The twin lead was kept at an electrically short VALUE to minimize the impact of the mismatching impedances and any attenuation. Ideally, in future work, this length could be reduced as a means to improve measurement accuracy.
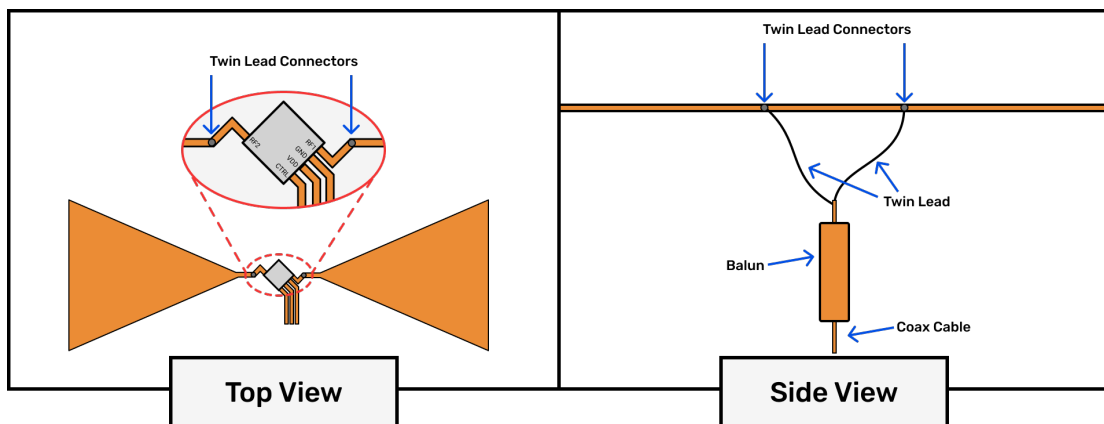

Figure 5.6: Model of the bowtie updated to include the twin lead connectors
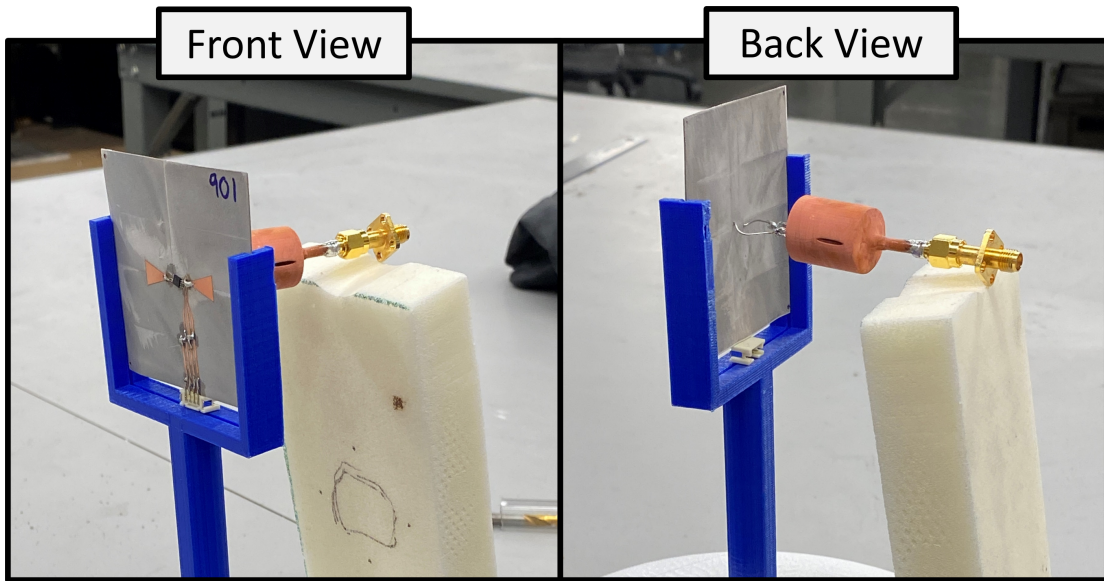
60

Figure 5.7: Picture of the bowtie loaded with the switch, twin leads, and balun

5.3.1 Balun Design, Fabrication, and Performance

In Figures 5.6 and 5.7, a balun is shown attached to the semi-rigid coax just before the twin lead. As Figure 5.8 shows, the balun acts as an RF choke, forcing any current off the exterior side of the coax's outer conductor [22]. If the balun were not present, then current could run along both the exterior and inner walls of the outer conductor, which would make the system unbalanced. Keeping the system balanced is vital as the bowtie is an example of a balanced structure, which means that the bowtie is most efficient when any current along the structure's two halves are equal in magnitude. If the current is allowed on the exterior wall of the outer conductor, then it will be impossible for the magnitude of any current on the bowtie halves to be equal, thus hindering performance. Additionally, if the system is left unbalanced, then the currents along the outer shield can form a common mode current and cause the coax to interfere with the antenna's radiation pattern.
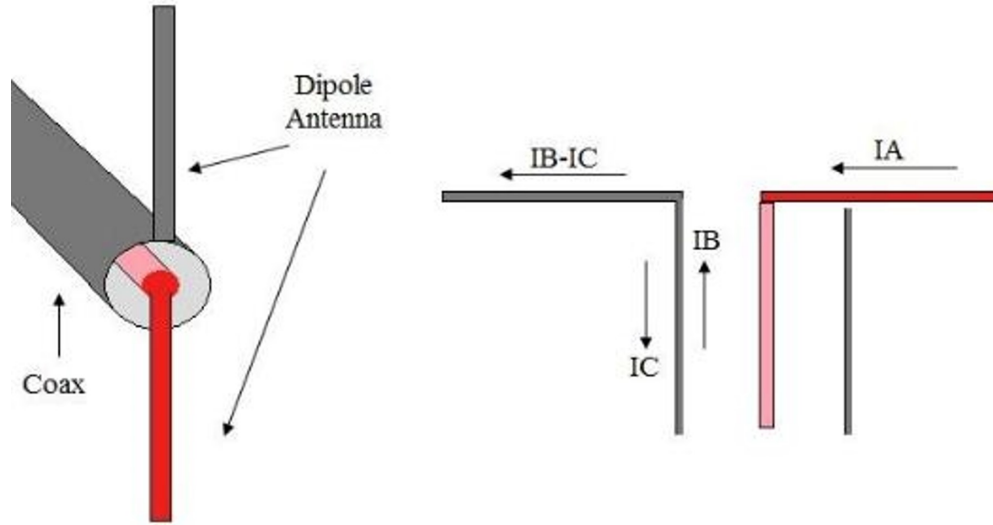
Figure 5.8: Diagram of a balun and the function it plays in chocking current on the outer conductor's exterior. [22]

The coax should be considered a three-port network when evaluating a balun, as shown in Figure 5.8. Treating the coax as a three-port network allows one to evaluate the balun's ability to choke current at a given frequency via the common-mode rejection ratio, CMRR, which is a ratio of S_{11}, S_{21}, and S_{31} performance and is expressed as,

$$CMRR = \frac{|S_{c1}|}{|S_{d1}|} \ . \tag{5.4}$$

Where,

$$S_{c1} = \frac{1}{\sqrt{2}} \left(S_{21} - S_{31}\right) \ ,$$

$$S_{d1} = \frac{1}{\sqrt{2}} \left(S_{21} + S_{31}\right) \ .$$

A higher CMRR indicates a greater choke. Ideally, the balun should offer a CMRR

value above 25 dB to be considered an efficient RF choke at a given frequency. The balun used for the effective aperture measurements was designed in HFSS to operate at 3 GHz with a CMRR peaking at 3.1 GHz [23]. This "over tuning" was done to account for the fabrication tolerances involved with a 3-D printed balun, as printed baluns tend to be tuned to a lower frequency. The realized CMRR is also shown in Figure 5.10, wherein it is shown peaking at just above 2.9 GHz and offering a CMRR above 25 dB from 2.6 to 3.2 GHz.
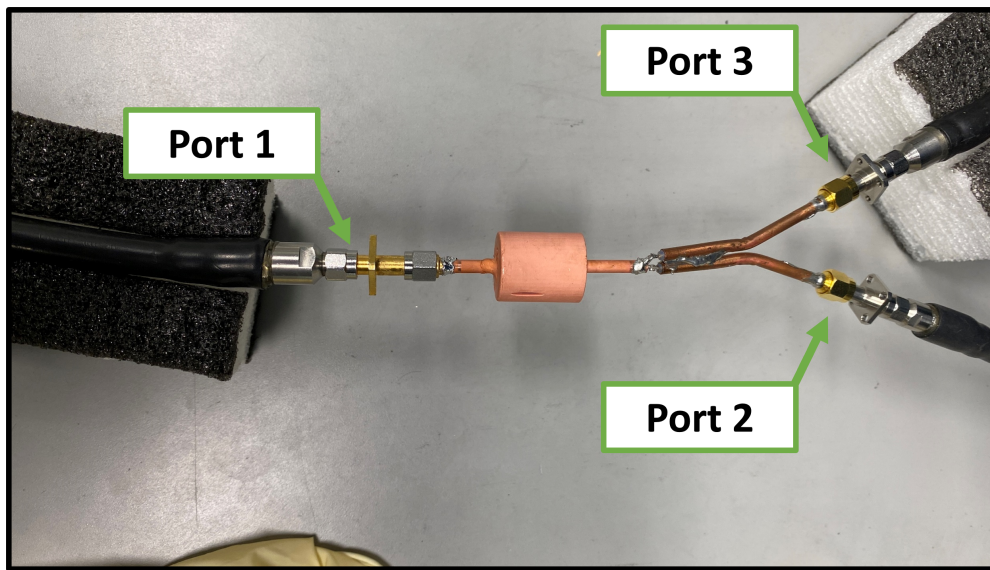

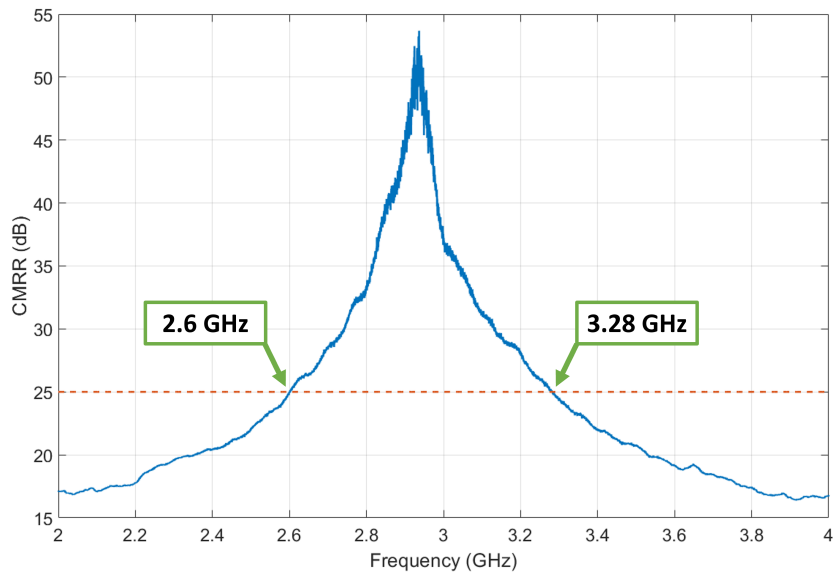Figure 5.9: A balun with a jig attached to the post balun end of the coax.

Figure 5.10: The 3 GHz balun's measured CMRR.

5.4   Cross-Frequency Effective Aperture Measurements

The following section presents the cross-frequency effective aperture measurements of the two time-varying antennas presented in the previous section. Each antenna is loaded with either the absorptive ADG901 or reflective ADG902 switch. The effective aperture of both devices is measured during cases when the time-varying load operates at four different frequencies, 4, 5, 10, and 20 MHz. Additionally, each time-varying measurement is compared to the effective aperture of the device when the switch is open or closed. This comparison serves as a control and highlights the impact of the time-varying loading on the device's performance.

5.4.1 The ADG901 Antenna's Cross-Frequency Effective Aperture

In the ADG901 loaded measurements shown in Figures 5.11, 5.12, 5.13, and 5.14, the two control cases expectedly provide only a response at the excitation frequency of 3 GHz. In the time-varying cases, responses can be seen at multiple frequencies including the excitation frequency. During the higher time-varying cases, Figures 5.13 and 5.14, the switch begins producing noise which is reflected in the "TV Noise" plot as there was no excitation provided during that measurement.
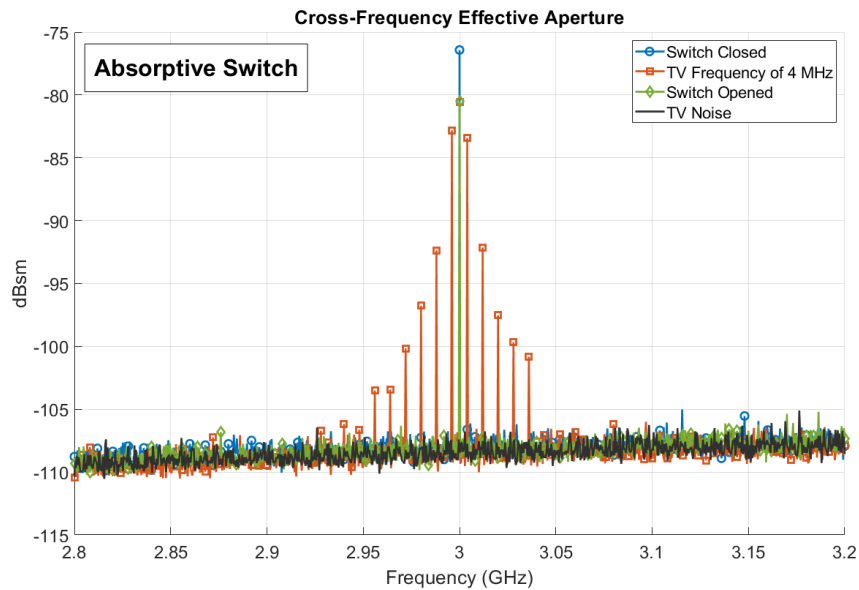

Figure 5.11: Cross-Frequency effective aperture of the bowtie while the absorptive switch opens and closes at a rate of 4 MHz.
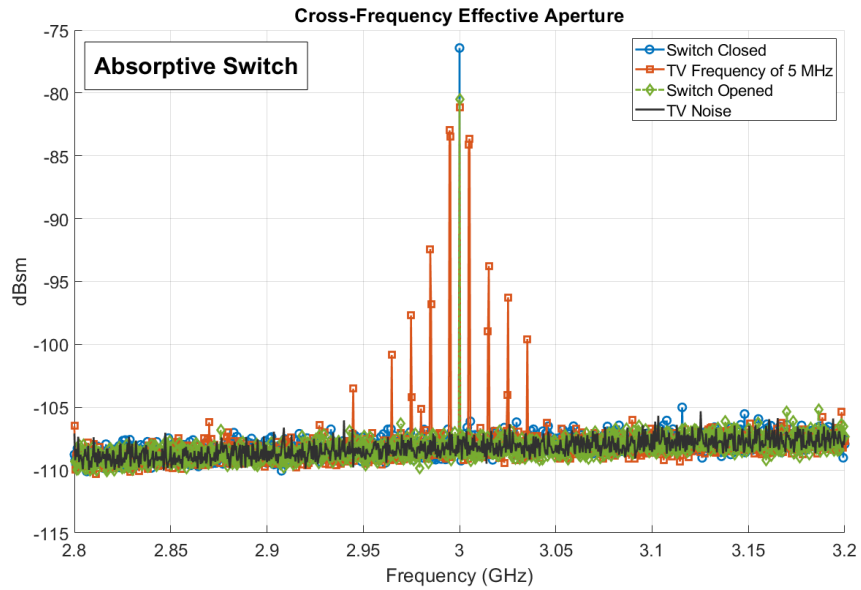
Figure 5.12: Cross-Frequency effective aperture of the bowtie while the absorptive switch opens and closes at a rate of 5 MHz.

Figure 5.13: Cross-Frequency effective aperture of the bowtie while the absorptive switch opens and closes at a rate of 10 MHz.

66

Figure 5.14: Cross-Frequency effective aperture of the bowtie while the absorptive switch opens and closes at a rate of 20 MHz.

5.4.2 The ADG902 Antenna's Cross-Frequency Effective Aperture

In the ADG902 loaded measurements shown in Figures 5.15, 5.16, 5.17, and 5.18, the two control cases again provide only a response at the excitation frequency of 3 GHz. In the time-varying cases, responses can be seen at multiple frequencies including the excitation frequency. During one of the higher time-varying cases, Figure 5.14, the switch begins producing noise which is reflected in the "TV Noise" plot as there was no excitation provided during that measurement.

Figure 5.15: Cross-Frequency effective aperture of the bowtie while the reflective switch opens and closes at a rate of 4 MHz.

Figure 5.16: Cross-Frequency effective aperture of the bowtie while the reflective switch opens and closes at a rate of 5 MHz.
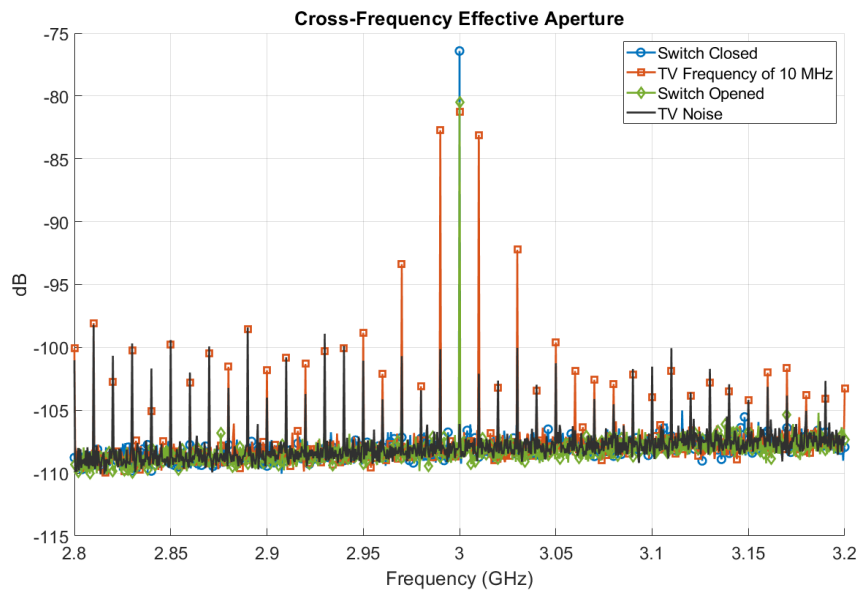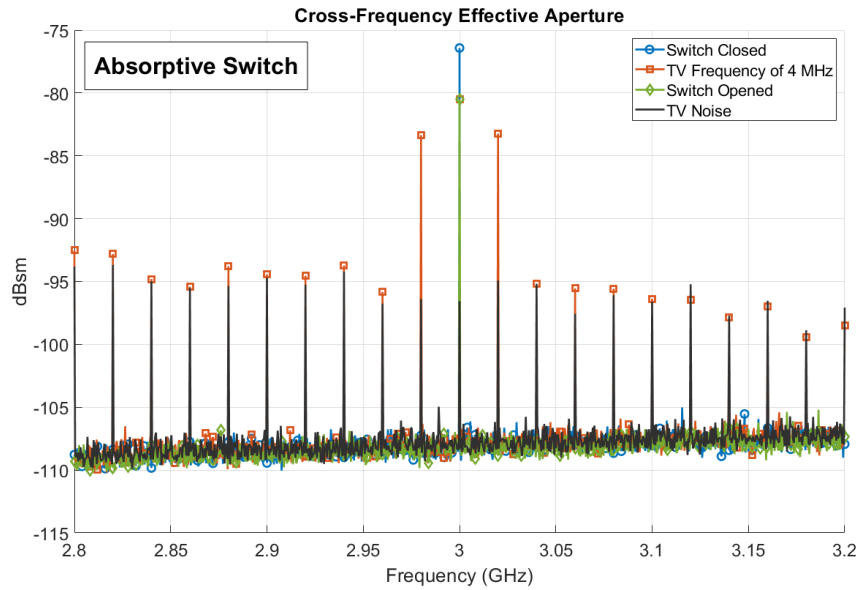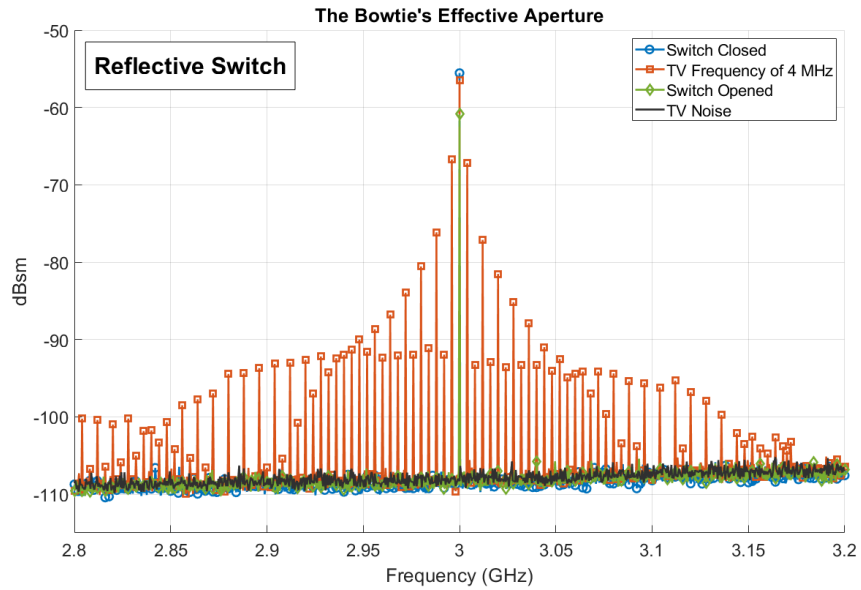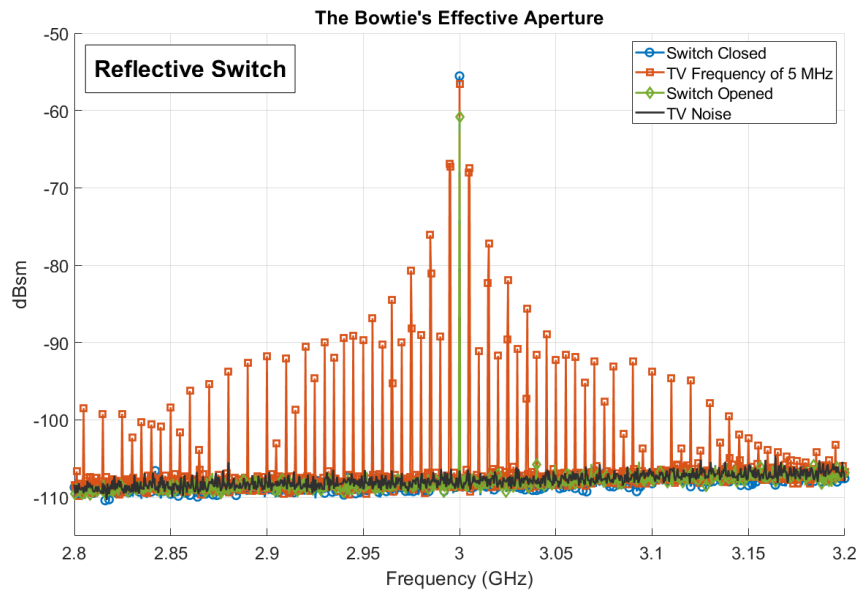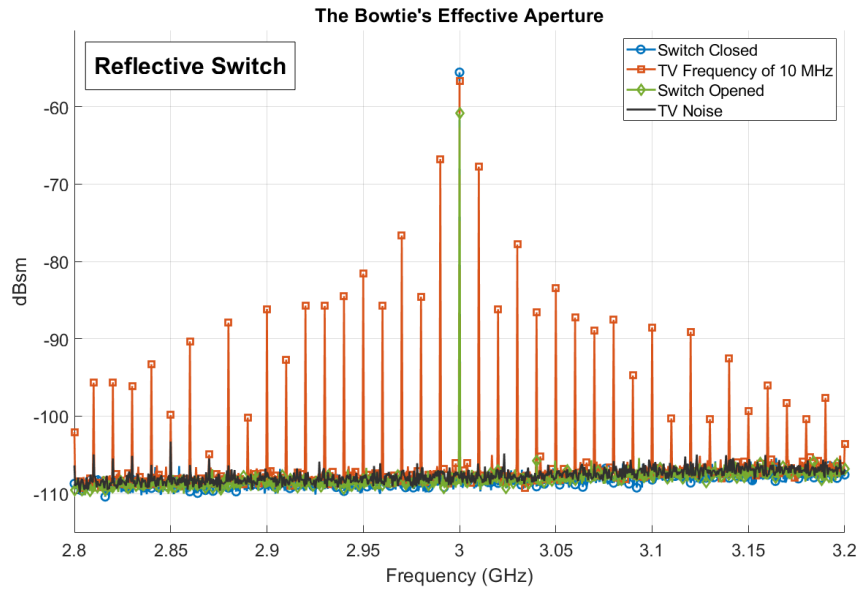
Figure 5.17: Cross-Frequency effective aperture of the bowtie while the reflective switch opens and closes at a rate of 10 MHz.
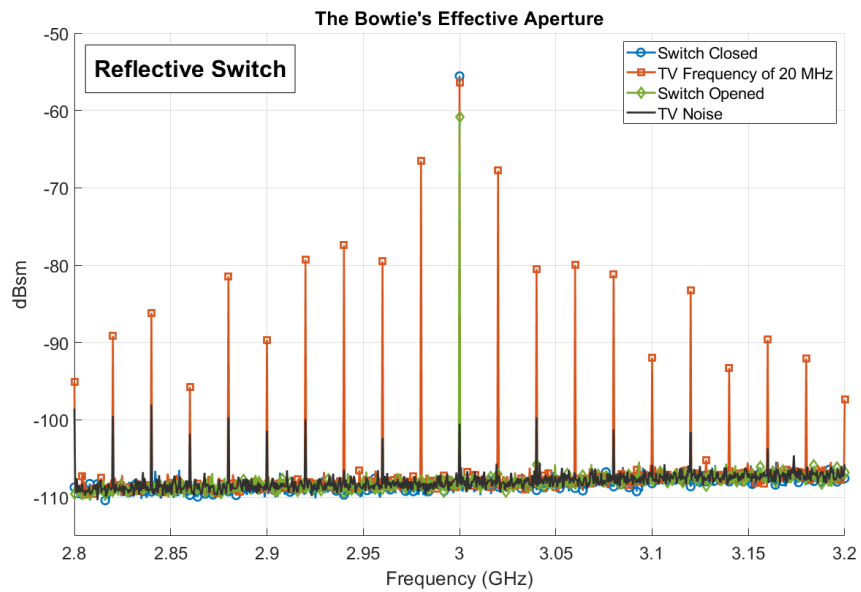

Figure 5.18: Cross-Frequency effective aperture of the bowtie while the reflective switch opens and closes at a rate of 20 MHz.

5.5 Discussion on Measurement and Simulation Comparisons

The measurements shown in the previous section must be supported by simulations to validate the effective aperture methodology. In the previous chapter both XFdtd and CM-MoM we utilized to validate the backscatter methodology. However, in this chapter only XFdtd is utilized since it was shown in the prior chapter that XFdtd and CM-MoM consistently agree with CM-MoM.

5.5.1 The ADG901 Antenna Measurements vs Simulations

The 901 loaded bowtie measurements showed sufficient agreement with the XFdtd simulation results. Both datasets agreed on the location and amplitude of every harmonic. There is a disagreement at the excitation frequency that will be addressed in the 902 loaded bowtie comparisons. It would seem given the agreement between the datasets that the measurement methodology is capable of producing accurate measurements of a device with a device loaded with an absorptive time-varying load.

Figure 5.19: The measured cross-frequency effective aperture of the absorptive bowtie equipped with a time-varying frequency of 4 MHz.

Figure 5.20: The measured cross-frequency effective aperture of the absorptive bowtie equipped with a time-varying frequency of 5 MHz.
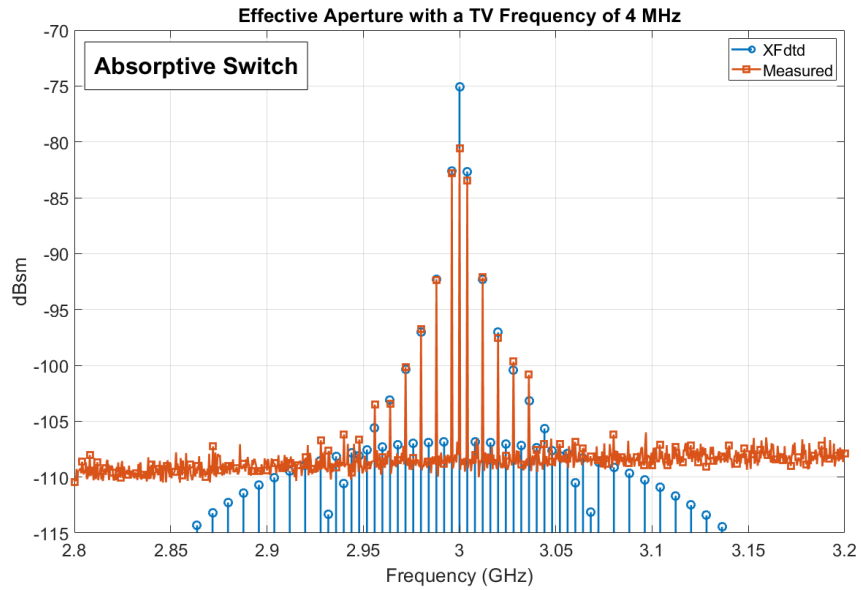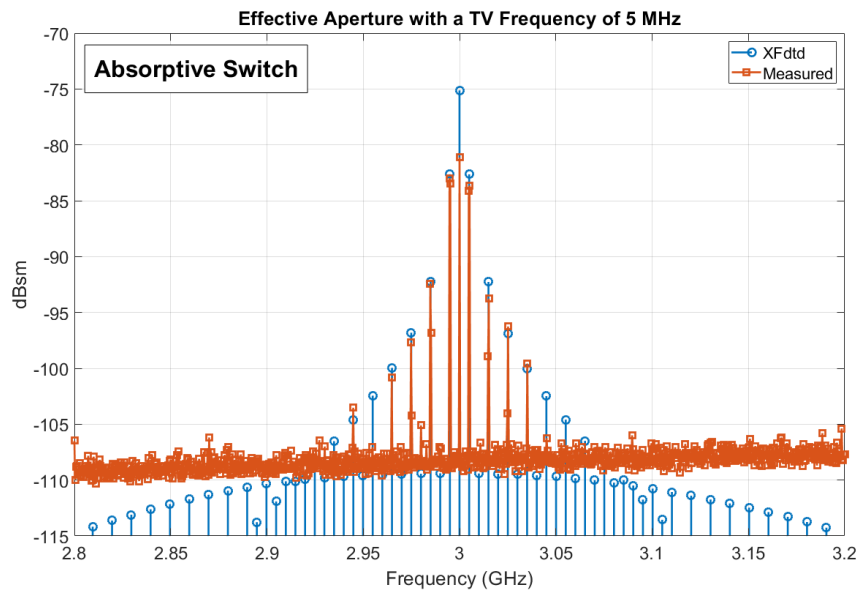
Figure 5.21: The measured cross-frequency effective aperture of the absorptive bowtie equipped with a time-varying frequency of 10 MHz.

Figure 5.22: The measured cross-frequency effective aperture of the absorptive bowtie equipped with a time-varying frequency of 20 MHz.

5.5.2   The ADG902 Antenna Measurements vs Simulations

Compared to the expected, the effective aperture measurements of the 902 loaded bowtie showed ample agreement. The most significant agreement is found regarding the location and magnitude of the harmonics. The most significant disagreement is found regarding the magnitude of the excitation response. The relationship between the excitation and the first harmonic was introduced in Chapter 4 as dependent on the average value of the simulation's switch. Despite knowing the source of the excitation as an issue with the switch and coax load model in XFdtd, fully addressing it is left to future work due to the long duration of XFdtd simulations and the need for a methodology to identify a proper model of the coax and switch loads in parallel. Additionally, the measurements report harmonics with asymmetry about the excitation frequency, a trend that was also seen in the backscatter measurements. However, despite these discrepancies, the measurement methodology would appear capable of producing results accurate to the expected of simulations.

Figure 5.23: The measured cross-frequency effective aperture of the absorptive bowtie equipped with a time-varying frequency of 4 MHz.

Figure 5.24: The measured cross-frequency effective aperture of the absorptive bowtie equipped with a time-varying frequency of 5 MHz.
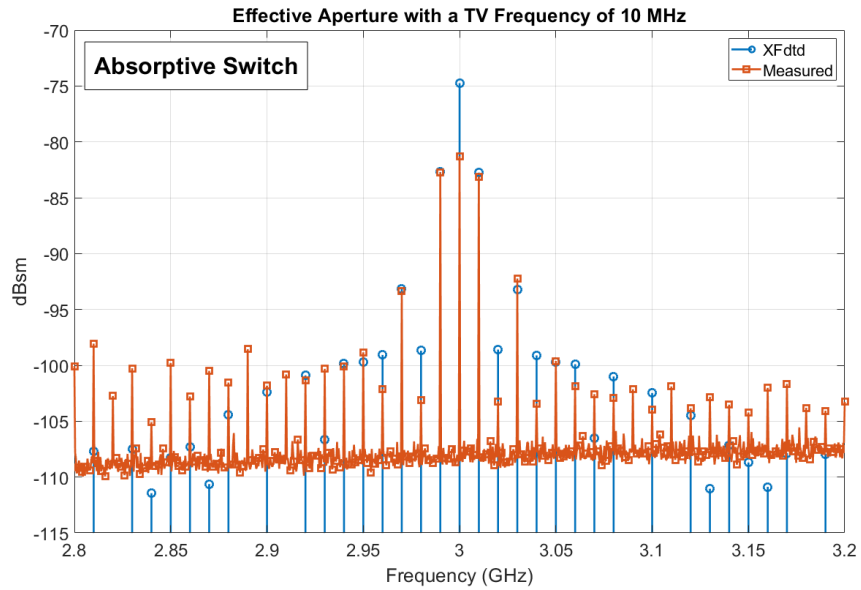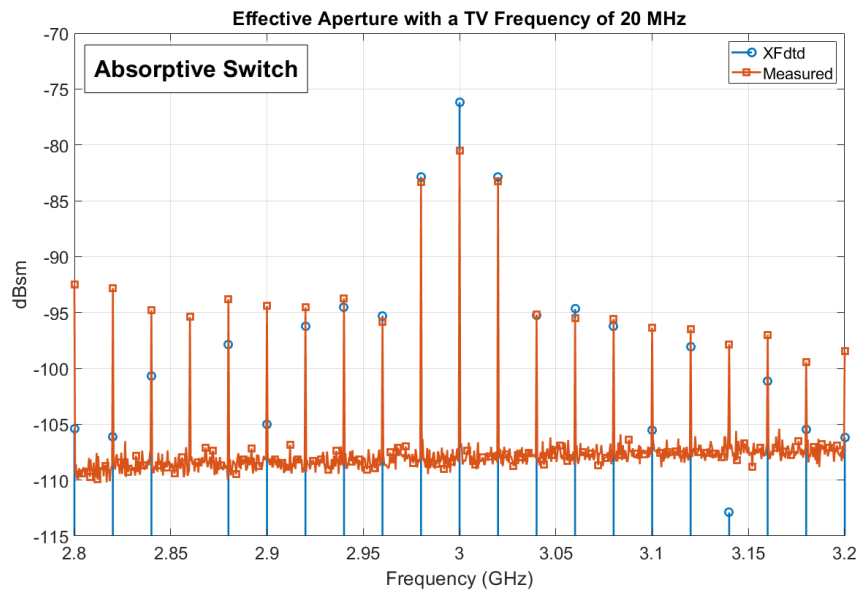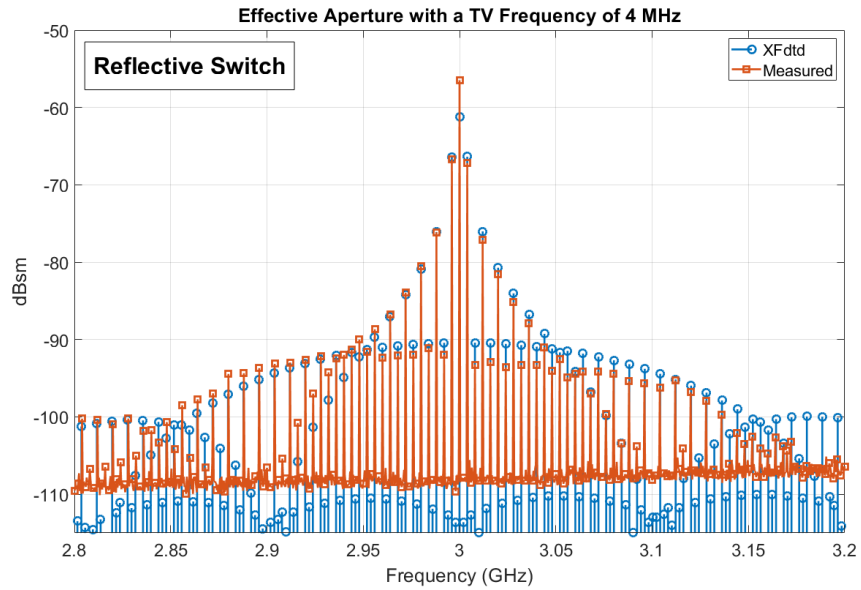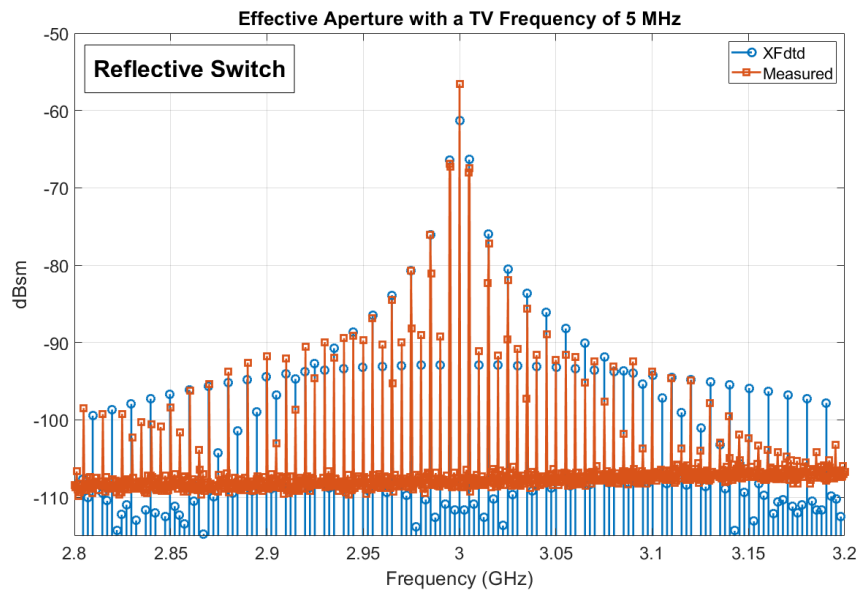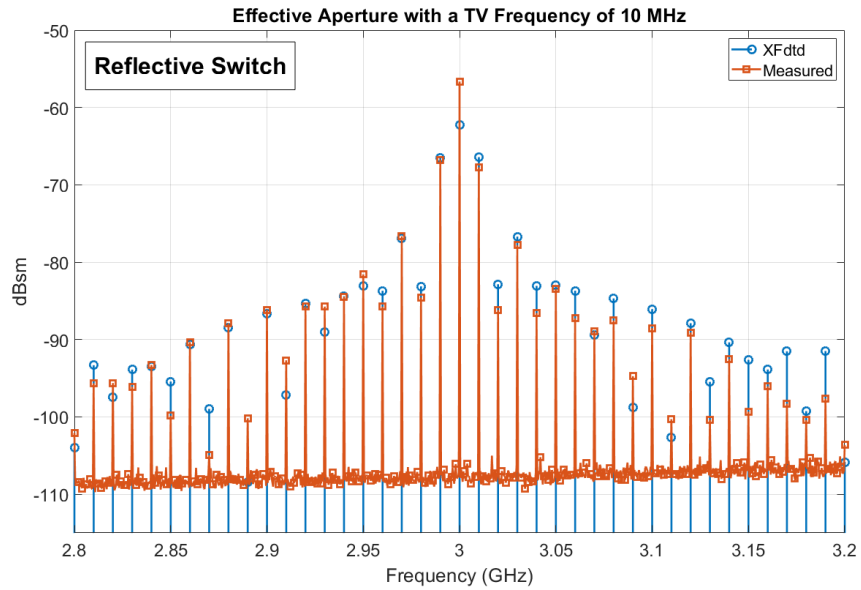
Figure 5.25: The measured cross-frequency effective aperture of the absorptive bowtie equipped with a time-varying frequency of 10 MHz.
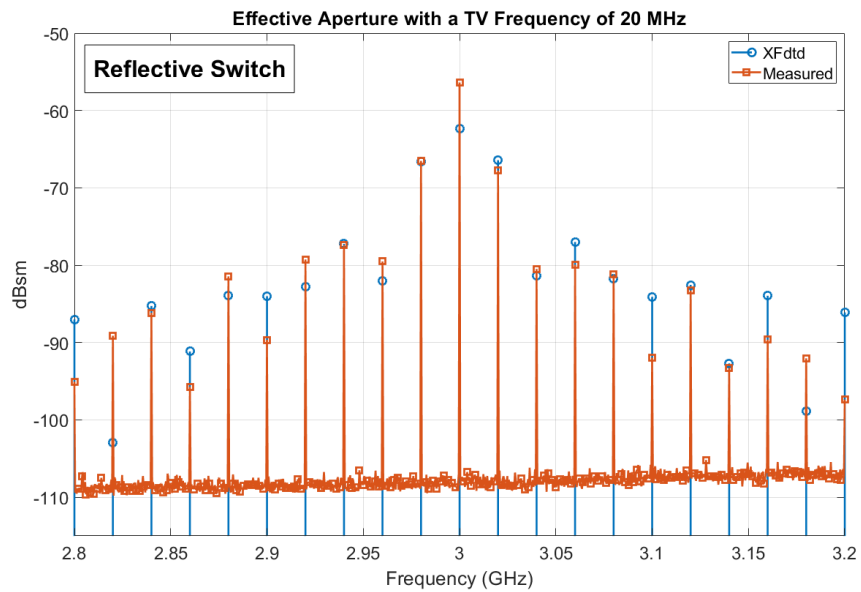

Figure 5.26: The measured cross-frequency effective aperture of the absorptive bowtie equipped with a time-varying frequency of 20 MHz.

Chapter 6

Conclusion and Future Work

The need for non-LTI forms of convectional antenna parameters and measurement methodologies has been addressed in this thesis as a mounting issue for the time-varying community. Before this thesis, measurements of time-varying scatterers and radiators were left uncalibrated as standard antenna parameters operate under time-invariant assumptions. A novel form of monostatic backscatter and effective aperture, two parameters often used to calibrate realized antenna performance, have been presented. The modified forms are denoted as cross-frequency in reference to their ability to capture the expected multiple frequency response of a time-varying device given a pure-toned excitation. Both terms required their own unique set of measurement methodology, which were developed from the ground up and presented. The methodologies were applied on a time-varying loaded bowtie, and the resulting measurements are presented in this thesis. The result of those measurements are supported by two electromagnetic solvers, which notably derive their results using a method different from the others. The time-varying antenna community can utilize these two terms and their methodologies to accurately quantify the realized performance of a time-varying antenna.

While both methodologies have been shown to produce measurements supported by simulations, the current effective aperture measurements have a source of error that

needs to be addressed. Currently, only the receive losses at the excitation frequency are calibrated out, which is an issue since the receive losses are frequency dependent. Thus, someone should address this issue by developing a method for extracting the receive chain losses individually to be calibrated appropriately from the effective aperture measurement. It might also be beneficial to confirm that the CM-MoM solver and XFdtd do, in fact, agree on the effective aperture measurements. A more accurate model of the parallel switch and coax should also be developed and implemented into XFdtd to address the observed excitation frequency disagreements.

It would benefit the time-varying community to adapt additional frequency parameters for time-varying devices. Specifically, it would be beneficial to the community for someone to continue adapting conventional frequency parameters to time-varying antennas. More specifically, a transmit term would be of interest as neither backscatter or effective aperture can be used to calibrate the transmission capabilities of a loaded time-varying antenna. Finally, it would be helpful to apply the current methodologies to additional time-vary scatterers and antennas to further validate their accuracy.

References

[1] L. J. Chu, "Physical limitations of omni-directional antennas," *Journal of applied physics*, vol. 19, no. 12, pp. 1163–1175, 1948.

[2] H. A. Wheeler, "Fundamental limitations of small antennas," *Proceedings of the IRE*, vol. 35, no. 12, pp. 1479–1484, 1947.

[3] S. R. Best, "A discussion on the quality factor of impedance matched electrically small wire antennas," *IEEE Transactions on Antennas and Propagation*, vol. 53, no. 1, pp. 502–508, 2005.

[4] J. S. McLean, "A re-examination of the fundamental limits on the radiation q of electrically small antennas," *IEEE Transactions on antennas and propagation*, vol. 44, no. 5, p. 672, 1996.

[5] H. Schuman, "Time-domain scattering from a nonlinearly loaded wire," *IEEE Transactions on Antennas and Propagation*, vol. 22, no. 4, pp. 611–613, 1974.

[6] T. Liu and F. Tesche, "Analysis of antennas and scatterers with nonlinear loads," *IEEE Transactions on Antennas and Propagation*, vol. 24, no. 2, pp. 131–139, 1976.

[7] J. Landt, E. Miller, and F. Deadrick, "Time domain modeling of nonlinear loads," *IEEE Transactions on Antennas and Propagation*, vol. 31, no. 1, pp. 121–126, 1983.

[8] C.-C. Huang and T.-H. Chu, "Analysis of wire scatterers with nonlinear or time-harmonic loads in the frequency domain," *IEEE transactions on antennas and propagation*, vol. 41, no. 1, pp. 25–30, 1993.

[9] T. Liu, F. Tesche, and F. Deadrick, "Transient excitation of an antenna with a nonlinear load: Numerical and experimental results," *IEEE Transactions on Antennas and Propagation*, vol. 25, no. 4, pp. 539–542, 1977.

[10] M. Salehi, "Time-varying small antennas for wideband applications," Ph.D. dissertation, Virginia Polytechnic Institute and State University, 2013.

[11] E. F. Knott, J. F. Schaeffer, and M. T. Tulley, *Radar cross section*. SciTech Publishing, 2004.

[12] R. E. Jarvis, J. G. Metcalf, J. E. Ruyle, and J. W. McDaniel, "Measurement and signal processing techniques for extracting highly accurate and wideband rcs," in *2021 IEEE International Instrumentation and Measurement Technology Conference (I2MTC)*, IEEE, 2021, pp. 1–6.

[13] M. I. Grace, *Measurement of radar cross section using the "VNA Master" handheld VNA*.

[14] B. R. Mahafza, *Radar Systems Analysis and Design Using MATLAB*, Third. CRC Press, 2013.

[15] R. Jarvis, "Calibration and clutter cancellation techniques for accurate wideband radar cross section measurements," 2021.

[16] S. Bass, A. Palmer, K. Schab, K. Kerby-Patel, and J. Ruyle, "Conversion matrix method of moments for time-varying electromagnetic analysis," *arXiv preprint arXiv:2103.06135*, 2021.

[17] Simulator, *Xfdtd*, 2020.

[18] C. A. Balanis, *Antenna theory: analysis and design*. John wiley & sons, 2015.

[19] A. Devices, "Hz to 4.5 ghz, 40 db off isolation at 1 ghz, 17 dbm p1db at 1 ghz spst switches," *Rev. D*,

[20] Verspecht and D. Root, "Polyharmonic distortion modeling," *IEEE Microwave Magazine*, vol. 7, no. 3, pp. 44–57, 2006. DOI: 10.1109/MMW.2006.1638289.

[21] *Measurements of ac magnitude: Basic ac theory: Electronics textbook*. [Online]. Available: https://www.allaboutcircuits.com/textbook/alternating-current/chpt-1/measurements-ac-magnitude/.

[22] P. Bevelacqua, "Antenna-theory. com," *Availabe online: http://www. antenna-theory. com/basics/friis. php (accessed on 26 December 2018)*, 2017.

[23] H. F. S. Simulator, *Hfss*, 2018.